Published OnlineFirst October 12, 2012; DOI: 10.1158/0008-5472.CAN-12-0088

In the present study, we focused on MSC–endothelial cell (EC) adhesion following TNF-α stimulation in an attempt to elucidate the mechanism of MSC accumulation at tumors.

Materials and Methods

Cell culture

Bone marrow–derived human MSCs (Lonza Walkersville, Inc.) were cultured in mesenPRO RS medium (Invitrogen). HEK293-derived AD-293 cells (Stratagene), human embryonic fibroblasts WI-38 (RIKEN BRC), human colon adenocarcinoma cell lines SW480 (Cell Resource Center for Biomedical Research Institute of Development, Aging and Cancer, Tohoku University, Miyagi, Japan), and SW480/RFP that was generated by transduction of SW480 with red fluorescent protein-expressing retrovirus vectors (RV-RFP), were grown in Dulbecco's Modified Eagle's Medium (DMEM)/F-12 medium (Invitrogen) supplemented with 10% FBS, 100 U/mL penicillin, and 100 μg/mL streptomycin (P/S). Human endothelial progenitor cells (ApproCell Inc.) were cultured in endothelial progenitor cells grown medium (ApproCell Inc.). Human colon adenocarcinoma cell lines Colo205 (Cell Resource Center for Biomedical Research Institute of Development, Aging and Cancer Tohoku University) and Colo205/RFP that was generated by transduction with RV-RFP, were grown in RPMI medium (Invitrogen) supplemented with FBS and P/S. All cultures were kept in an incubator at 37°C and 5% CO_2.

Adenoviral vectors

Adenoviral vectors expressing a GFP were constructed by an improved *in vitro* ligation method (8, 9). The shuttle plasmid pHMCA5-GFP contains a CA promoter (a β-actin promoter/CMV enhancer with a β-actin intron), *GFP* gene, and a bovine growth hormone (BGH) polyadenylation signal, all of which are flanked by I-CeuI and PI-SceI restriction sites. I-CeuI/PI-SceI–digested pHMCA5-GFP was ligated with I-CeuI/PI-SceI–digested pAdHM4, resulting in pAdHM4-CAGFP. pAdHM41-K7-CAGFP was constructed by ligation of I-CeuI/PISceI–digested pHMCA5-GFP with I-CeuI/PI-SceI–digested pAdHM41-K7 (10). Viruses (Ad5-GFP and AdK7-GFP) were generated by transfection of PacI-digested pAdHM4-CAGFP and pAdHM41-K7-CAGFP, respectively, into AD-293 cells with SuperFect (Qiagen) according to the manufacturer's instructions. Each virus was purified by $CsCl_2$ step gradient ultracentrifugation followed by $CsCl_2$ linear gradient ultracentrifugation. Virus particles and biologic titers of each vector preparation were determined as described by Mittereder and colleagues (11). We also created Ad vectors expressing luciferase (Luc) using the shuttle plasmid pHMCA5-Luc, which contains the *Luc* gene derived from pELuc-test (Toyobo Co. Ltd.). MSCs and fibroblasts were seeded in culture plates or flasks at a density of 1×10^4 cells/cm^2, and the next day the cells were treated with each adenovirus vector for 1.5 hours. The medium containing the vectors was removed and replaced with fresh medium.

Animal models

All animal experiments were approved by the Jichi Medical University (Tochigi, Japan) ethics committee and carried out in accordance with the NIH Guide for the Care and Use of Laboratory Animals. To create tumor-bearing mice, SW480/RFP cells (3×10^6) were subcutaneously inoculated into 4- to 6-week-old male Balb/c nu/nu mice (Clea Japan Inc.). The mice were used for experiments 7 days after inoculation.

Immunohistochemistry

Cultured MSCs and fibroblasts were transduced with AdK7-GFP at a concentration of 3,000 virus particles per cell (vp/cell). Two days after transduction, cells were injected into the left ventricular cavities (1×10^6, day 0) of tumor-bearing mice. Mice were sacrificed on day 4, and 7-μm serial cryosections from frozen tissues were processed. Immunohistochemistry was conducted with fluorescein isothiocyanate (FITC)-conjugated anti-GFP antibody (ab6662; Abcam Inc.) on tumor cryosections to detect MSCs or fibroblasts. Nuclei were stained with 4′,6-diamidino-2-phenylindole (DAPI; Vector Laboratories, Inc.). Images were obtained with a fluorescence microscope (BZ-9000; Keyence). SW480/RFP cells (3×10^6) were subcutaneously inoculated into 4- to 6-week-old male Balb/c nu/nu mice. Mice were sacrificed on day 11, serial sections from tumor tissues were processed. Immunohistochemistry was conducted with anti-mouse CD34 monoclonal antibody (MEC14.7; GeneTex Inc.) on tumor section to detect tumor blood vessels. Histofine Simple Stain Mouse MAX PO (Nichirei Biosciences, Inc.) was used as a horseradish peroxidase–conjugated secondary antibody, and 3,3′-diaminobenzidine (DAB) solution was used for brown color development. Sections were then counterstained with Hematoxylin (Wako Pure Chemical Industries, Ltd.). Images were obtained with a fluorescence microscope (BZ-9000).

In vivo imaging of homing ability to tumors

Cultured MSCs and fibroblasts were transduced with AdK7-Luc at a concentration of 3,000 and 680 vp/cell, respectively. Two days after transduction, cells were injected into the left ventricular cavities (1×10^6, day 0) of tumor-bearing mice, and then optical bioluminescence imaging was conducted to periodically trace the cells using an *in vivo* imaging system (IVIS; Xenogen). To detect bioluminescence from MSCs or fibroblasts, the reporter substrate D-luciferin (Ieda Chemical Co., Ltd.) was injected into the mouse peritoneum (75 mg/kg body weight) for scanning. The luminescent intensity at tumor sites was analyzed using Living Image software (Xenogen).

In vitro migration assays

Cultured MSCs or fibroblasts were serum-starved for 12 hours. One hundred microliters of tumor conditioning medium (CM), or serum-free medium supplemented with PDGF-BB (10 ng/mL), HGF (30 ng/mL), fibroblast growth factor-β (FGF-β; 20 ng/mL), SDF-1α (150 ng/mL), VEGF-A (25 ng/mL), or monocyte chemoattractant protein-1 (MCP-1; 100 ng/mL) was added to the lower wells of migration chambers (8-μm pore size; Neuro Probe, Inc.); MSCs or fibroblasts (4×10^4) were added to the upper wells. All recombinant proteins were purchased from R&D systems Inc.. Medium alone (DMEM/F-12) was used as a negative control and treatment with 30% FBS was the positive control. After incubation for 24 hours at

Published OnlineFirst October 12, 2012; DOI: 10.1158/0008-5472.CAN-12-0088

37°C, cells were labeled with CyQUANT NF dye, and cells attached to the lower surface of the filters were detached with trypsin. Fluorescent intensity was measured using a fluoroscan, and the number of adherent cells was quantified using a standard curve constructed by a known number of cells.

Flow cytometric analysis of adhesion molecules

Cultured MSCs, fibroblasts or endothelial cells were stimulated with TNF-α and harvested by trypsinization. Cell aliquots were incubated with FITC-conjugated monoclonal antibodies (BD) against vascular cell adhesion molecule-1 (VCAM-1), CD49d, CD29 (Integrin-β1), and analyzed by flow cytometry (FACScan; BD Biosciences). For each analysis, an aliquot of cells was also stained with isotype control immunoglobulin G (IgG)–conjugated to FITC as a negative control.

Assay for TNF-α produced in tumor-bearing mice

SW480/RFP (3×10^6) cells were subcutaneously inoculated into nude mice. Seven days after inoculation, mice were anesthetized with an overdose of isoflurane inhalation. The blood was collected and allowed to coagulate overnight on ice. After centrifugation of the samples (2,000 × *g*, 30 minutes, 4°C), the serum was removed and stored at −70°C. Tumor, spleen, and liver tissues were homogenized in 1.5 mL of α-minimum essential medium using a tissue homogenizer. The homogenates were then centrifuged (2,000 × *g*, 30 minutes, 4°C), and the supernatant was removed and recentrifuged (14,000 × *g*, 30 minutes, 4°C). Serum and supernatants from tissue homogenates were kept at −70°C until use. TNF-α was assayed using a commercially available ELISA kit (mouse TNF-α Instant ELISA; Bender MedSystems) according to the manufacturer's protocols.

***In vitro* adhesion assays**

For adhesion assays, endothelial cells (at 4 passages) were cultured to confluence on fibronectin-coated 96-well plates (20 ng/mL; Sigma-Aldrich, Inc.) and treated with TNF-α (10 ng/mL) for 12 hours before assaying. MSCs and fibroblasts were treated with TNF-α (10 ng/mL) 12 hours before the adhesion assays and incubated with isotype control IgG or anti-VCAM-1 or very late antigen-4 (VLA-4; 10 μg/mL) monoclonal antibodies (mAb) for 1 hour. Cells were labeled with CyQUANT NF dye, and 1×10^4 cells were seeded onto endothelial cells. After 30 minutes of incubation at 37°C, wells were washed thoroughly 3 times with PBS to remove nonadherent cells. Fluorescent intensity was measured using a fluoroscan, and the number of adherent cells was quantified using a standard curve constructed by a known number of cells. In some experiments, MSCs and fibroblasts were pretreated for adhesion studies with one of the following substances: TNF-α (10 ng/mL), anti-VCAM-1 antibody (mouse monoclonal anti-rat, clone 5F10, 10 μg/mL, Eurogentec), or anti-VLA-4 antibody (mouse monoclonal anti-rat, clone 1A29, 10 μg/mL, Research Diagnostics).

Parthenolide treatment of MSCs

Parthenolide (Biomol) was reconstituted in dimethyl sulfoxide (DMSO; Sigma-Aldrich, Inc.) to a stock concentration of 0.4 mol/L and subsequently diluted in PBS. MSCs were treated with parthenolide (5 μmol/L) for 6 hours before experiments. To assess the effect of parthenolide treatment of transgene expression, cells were reseeded into 96-well plates, and luciferase assays were conducted using luciferase-expressing MSCs. Cell viability after parthenolide treatment was also examined with Cell Proliferation Kit II [2,3-bis[2-methoxy-4-nitro-5-sulfophenyl]H-tetrazolium-5 carboxanilide inner salt (XTT); Roche Diagnostics GmbH] according to the manufacturer's instructions.

Western blotting

Western blot analysis was conducted to measure the NF-κB pathways. Next, MSCs were pretreated with parthenolide or vehicle (DMSO) for 6 hours, and then cultured with TNF-α (10 ng/mL) for 3 minutes. Cells were lysed in radioimmunoprecipitation assay (RIPA) buffer containing protease inhibitor (Pierce Biotechnology). Protein extracts were electrophoresed on a 4% to 12% Bis–Tris gel (Invitrogen), and transferred to polyvinylidene difluoride (PVDF) membranes. Membranes were incubated in PVDF blocking reagent (TOYOBO), and then incubated with primary antibodies against the following proteins: IκBα, phospho-IκBα (Ser32), NF-κB p65, phospho-NF-κB p65 (Ser536), and α-tublin (Cell Signaling Technology), followed by incubation with horseradish peroxidase-conjugated goat anti-rabbit IgG or -mouse IgG1 secondary antibody, and detected using a Western blotting detection system (GE Healthcare).

Immunocytochemistry

To visualize p65 nuclear translocation, MSCs were pretreated with parthenolide or vehicle (DMSO) for 6 hours and then cultured with TNF-α (10 ng/mL) for 20 minutes. Cells were fixed with 4% fomaline and permiabilized with Triron-X 100. After washing with PBS, slides were incubated with rabbit anti-p65 antibody (Cell Signaling Technology), followed by incubation with Alexa Fluor 488–conjugated goat anti-rabbit IgG secondary antibody. The actin cytoskeleton was stained with Alexa Fluor 546–conjugated phalloidin (Invitrogen); nuclei were stained with 1,5-bis{[2-(di-methylamino) ethyl]amino}-4,8-dihydroxyanthracene-9,10-dione (DRAQ)-5 dye (Invitrogen). Cells were examined using Keyence BZ-9000.

Results

***In vivo* imaging of MSC accumulation in tumors**

We used bone marrow–derived human MSCs, which expressed characteristic phenotypic markers for MSCs and differentiated into adipocyte, osteocyte, and chondrocyte under specific culture conditions (Supplementary Fig. S1). Then, fiber-modified adenovirus vectors (AdK7) were used for efficient transduction of MSCs and fibroblasts in this study. When the cells were transduced with GFP-expressing AdK7 vectors at a density of 3,000 vp/cell, transduction efficiency was almost 100% (Supplementary Fig. S2A and S2B). The bioluminescent intensity of MSCs transduced with luciferase-expressing Ad vectors at 3,000 vp/cell was equal to that of fibroblasts transduced at 680 vp/cell (Supplementary Fig. S2C). Mice injected with GFP-expressing MSCs or fibroblasts were sacrificed 4 days after injection for immunohistochemical analysis.

Published OnlineFirst October 12, 2012; DOI: 10.1158/0008-5472.CAN-12-0088

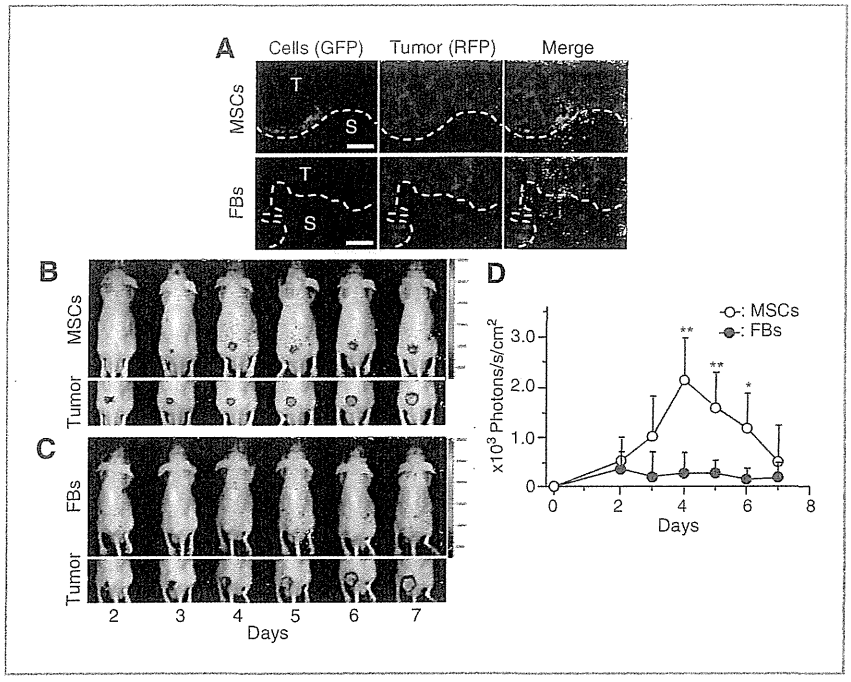

Figure 1. Tumor homing ability of MSCs *in vivo*. A, subcutaneous tumors were induced by injection of SW480/RFP cells (3×10^6) in nude mice (day 0). Cultured MSCs or fibroblasts were transduced with GFP-expressing adenovirus vectors 2 days before injection (day 5) and were injected into the left ventricular cavity (1×10^6, day 7). Mice were sacrificed on day 11, and immunohistochemistry was conducted with anti-GFP antibody on tumor cryosections to detect MSCs or fibroblasts. Top, fluorescent microscopy view of MSC detection; MSCs (left), RFP-labeled tumor cells (center), nucleic staining with DAPI and merge (right). Bottom, fluorescent microscopy view of fibroblast detection; fibroblasts (left), RFP-labeled tumor cells (center), nucleic staining with DAPI and merge (right). Data shown are from 1 representative experiment of 3 carried out. Scale bar, 100 μm. S, stroma; T, tumor. B, luciferase-expressing MSCs were injected into tumor-bearing mice via the left ventricular cavity (1×10^6, day 7). Optical bioluminescence imaging was conducted to periodically trace the cells using IVIS. Top, biodistribution of MSCs as detected by luminescence. Bottom, tumor site detected by red fluorescence. Data shown are from 1 representative experiment of 8 carried out. C, luciferase-expressing fibroblasts were injected into tumor-bearing mice and IVIS imaging was conducted as described earlier. Top, biodistribution of fibroblasts indicated by luminescence. Bottom, tumor site indicated by red fluorescence. Data shown are from 1 representative experiment of 7 carried out. D, bioluminescent intensity at tumor sites was quantified using analysis software. The data are expressed as mean ± SD ($n = 8$ for MSCs and $n = 7$ for fibroblasts). *, $P < 0.05$; **, $P < 0.01$ compared with fibroblasts at the same time.

MSCs identified with anti-GFP antibody were detected in the boundaries of tumors and tumor stroma. However, we found no GFP-positive fibroblasts in the tumor tissues (Fig. 1A). We also used bioluminescence imaging to quantitatively investigate the tumor tropism of MSCs. We injected luciferase-expressing MSCs or fibroblasts into mice through the left ventricular cavity, and then conducted optical bioluminescence imaging to periodically trace the cells using IVIS. In mice injected with luciferase-expressing MSCs, optical bioluminescence at tumor sites became pronounced over time (Fig. 1B), and signal intensity gradually increased (Fig. 1D). In contrast, we observed no signal at the tumor sites in mice injected with luciferase-expressing fibroblasts (Fig. 1C and D).

In vitro migration assays

We analyzed the effects of several growth factors (specifically PDGF-BB, HGF, and VEGF), chemokines (specifically MCP-1 and SDF-1α), and SW480 culture–conditioned medium on MSC and fibroblast migration. These factors are commonly expressed in tumor tissues, and are thought to be potential mediators of MSC tropism. We also used serum-free medium as a negative control and medium containing 30% FBS as a positive control. Migration was quantified by direct labeling and counting of cells by a fluorometer (Fluoroskan Ascent FL; Thermo Labsystems). Exposure to PDGF, HGF, or conditioned medium from SW480 cells stimulated significant MSC migration, whereas VEGF and SDF-1α had no significant effect as compared with serum-free medium (Fig. 2). We compared the migration capacity of MSCs and fibroblasts, the factors that attracted MSCs also induced migration of fibroblasts. Rather, it seems that fibroblasts were more strongly attracted to these factors than MSCs.

In vitro adhesion assays

The tumors generated in mice in this study strongly induced tumor stroma with defined blood vessels, and MSCs specifically accumulated in this stroma (Fig. 3A). Therefore, we propose a hypothesis as follows: factors, as indicated in Fig. 2, attract both MSCs and fibroblasts to the tumor microenvironment, but importantly, MSCs significantly adhere to endothelial cells as

Published OnlineFirst October 12, 2012; DOI: 10.1158/0008-5472.CAN-12-0088

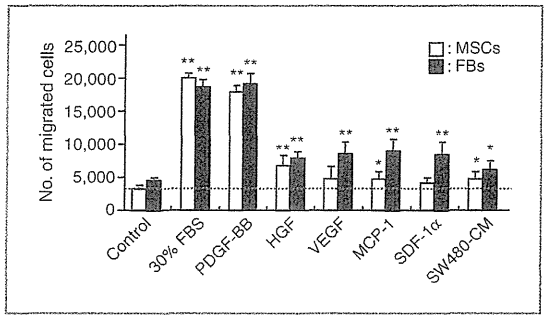

Figure 2. Migratory capacity of MSCs and fibroblasts (FB) in response to growth factors, chemokines, and conditioned medium from SW480 cells. MSCs or fibroblasts were serum-starved for 12 hours. Cells (4×10^4) were added to upper wells of migration chambers. Then, tumor conditioning medium, serum-free medium supplemented with PDGF-BB (10 ng/mL), HGF (30 ng/mL), SDF-1α (150 ng/mL), VEGF-A (25 ng/mL), or MCP-1 (100 ng/mL) were added to the lower wells. Treatment with medium alone (DMEM/F-12) was used as a negative control and treatment with 30% FBS was used as the positive control. The contents of the upper wells and lower wells were separated by polycarbonate filters (8 μm). The data are expressed as mean ± SD ($n = 8$ per cell type). Values are presented as mean ± SE. *, $P < 0.05$ and **, $P < 0.01$ compared with each control.

compared with fibroblasts. Therefore, only MSCs migrate and accumulate at tumor sites via blood vessels in tumor stroma. We speculated that inflammatory cytokines (specifically TNF-α) are required for induction of adhesion molecule expression. First, we measured TNF-α levels in tumor tissues by ELISA. The TNF-α level is significantly higher in tumor tissues as compared with liver and spleen (Fig. 3B). Similar results were also observed in another experiments using Colo205 tumor cells (Supplementary Fig. S3). Then, we assessed the expression of adhesion molecules on endothelial cells, MSCs, and fibroblasts by fluorescence-activated cell sorting analysis. After TNF-α stimulation, endothelial cells and MSCs significantly expressed adhesion molecules including VCAM-1 and VLA-4, compared with fibroblasts (Fig. 3C). We also examined the *in vitro* adhesion of MSCs to endothelial cells. MSCs effectively adhered to endothelial cells as compared with fibroblasts (Fig. 3D). Furthermore, this adhesion was partially inhibited by blocking antibodies against VCAM-1 and VLA-4.

Effects of parthenolide on MSC migration and adhesion

We propose a hypothesis that if TNF-α–induced VCAM-1 expression is inhibited, MSC accumulation at tumors is also attenuated. It is well known that TNF-α induces VCAM-1 expression through the NF-κB signaling pathway. We used parthenolide, a sesquiterpene lactone that occurs naturally in the Feverfew plant. Although parthenolide has several biologic activities, we focused on its suppressive effect on NF-κB activity. At first, there were no differences in migratory capacity toward growth factors or chemokines with or without parthenolide treatment (Fig. 4A). Next, we assessed the inhibitory effect of parthenolide on NF-κB activity: MSCs were pretreated for 6 hours, and then were stimulated with TNF-α for 3 minutes. Parthenolide suppressed p65 nuclear translocation through the inhibition of IκBα phosphorylation (Fig. 4B and C) and strongly inhibited the TNF-α–induced VCAM-1 expression on MSCs (Fig. 4D). Consequently, and MSC–EC adhesion was strongly inhibited by parthenolide treatment similarly to anti-VCAM-1 blocking antibody (Fig. 4E).

***In vivo* imaging of parthenolide-treated MSCs**

First, we examined the effect of parthenolide treatment on transgene expression and cell viability. There were no significant effects on transgene expression and cell viability after parthenolide treatment (Fig. 5A and B). Next, we conducted *in vivo* imaging using IVIS. We observed definite bioluminescence at tumor sites in the mice injected with untreated MSCs (Fig. 5C), and bioluminescent intensity was gradually increased (Fig. 5E), as indicated earlier (Fig. 1B). In contrast, we could not observe definite accumulation at the tumor sites in mice injected with parthenolide-treated MSCs (Fig. 5D and E). Similar results were also obtained by experiments using Colo205 tumor-bearing mice (Supplementary Fig. S4).

Discussion

In this study, we showed that MSC accumulation at tumor sites would be related not only to migratory capacity toward growth factors and chemokines, but also to MSC–EC adhesion following activation by TNF-α. We further showed that NF-κB activity regulates MSC accumulation at tumor sites through the induction of VCAM-1 expression and the resultant interaction with tumor blood vessel endothelial cells.

It is thought that MSCs are mobilized into action following tissue damage, such as injury or inflammation typically accompanied by the release of inflammatory cytokines from the damaged tissues, leading to the recruitment of MSCs to the target. Tumors have a microenvironment consisting of large numbers of inflammatory cells (12). This microenvironment promotes the recruitment of MSCs via various soluble factors secreted by the tumor and inflammatory cells, including EGF, VEGF-A, FGF, PDGF, SDF-1α, IL-8, IL-6, granulocyte colony-stimulating factor (G-CSF), granulocyte-macrophage colony-stimulating factor (GM-CSF), MCP-1, HGF, TGF-β1, and urokinase-type plasminogen activator (uPA; ref. 13). However, in our experimental settings, although systemically injected MSCs accumulated at the tumors, subcutaneously injected MSCs did not (data not shown). We also compared the migration capacity of MSCs and fibroblasts toward growth factors and chemokines *in vitro*. Rather, it seems that fibroblasts were more strongly attracted to these factors than MSCs. Our results suggest that the mechanism of MSC accumulation cannot be explained solely by cytokine-mediated migration. Therefore, we need different viewpoints to clarify the mechanism.

The tumors generated in this study strongly induced tumor stroma with large numbers of blood vessels, and MSCs in particular accumulated in the boundaries between the tumors and tumor stroma. Furthermore, MSC accumulation at the site of the tumors was observed only when cells were injected via the left ventricular cavity. Therefore, we focused on MSC–EC adhesion to elucidate the mechanisms involved.

It has previously been reported that the interaction of MSCs with the vascular endothelium resembles leukocyte chemotaxis (14). To analyze these interactions, we referred to a model

Published OnlineFirst October 12, 2012; DOI: 10.1158/0008-5472.CAN-12-0088

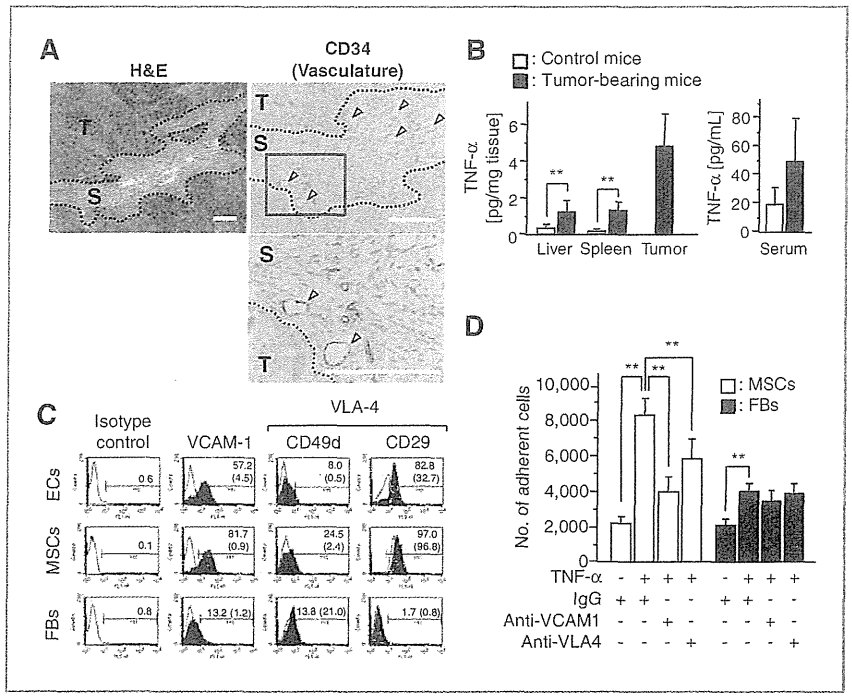

Figure 3. A, sections represent hematoxylin and eosin (H&E) staining (top left), the $CD34^+$ blood vessels/endothelial cells in tumor tissues (top right), the high-power field of view (bottom). Data shown are from 1 representative experiment of 3 carried out. Scale bar, 100 μm. S, stroma; T, tumor. B, specimens of tumor, liver, spleen, and blood were collected from control and tumor-bearing mice. TNF-α levels in tissue homogenates and serum were assayed by ELISA. *, $P < 0.05$; **, $P < 0.01$. C, MSCs, endothelial cells (EC), and fibroblasts were cultured with TNF-α (10 ng/mL) for 6 hours. Cells were labeled with FITC-conjugated antibodies and analyzed by flow cytometry (filled histogram). Rat isotype antibodies IgG1 and IgG2a served as respective controls (open histograms). Values represent the percentage of positive cells after TNF-α stimulation, and values in parentheses represent the percentage of positive cells without TNF-α stimulation. D, endothelial cells were cultured to confluence on fibronectin-coated 96-well plates. Then, MSCs or fibroblasts (1×10^4) were added to cultured endothelial cells. MSCs and endothelial cells were pretreated with the following substances: TNF-α (10 ng/mL), anti-VCAM-1, VLA-4 (10 μg/mL), or isotype control IgG. Values are mean ± SD. **, $P < 0.01$ ($n = 6$ per cell type).

that has been proposed for endothelial cell regulation of leukocyte infiltration in inflammatory tissues. Leukocyte-endothelial adhesion involves dynamic interactions between leukocytes and endothelial cells, and involves multiple steps. These steps must be precisely orchestrated to ensure a rapid response with minimal damage to healthy tissue (15). Interactions between leukocytes and the endothelium are mediated by several families of adhesion molecules, each of which participates in a different phase of the process. The surface expression and activation of these molecules during an inflammatory response is tightly controlled under normal conditions. Inflammatory cytokines including IL-1 and TNF-α involve induction of adhesion molecules. In our experimental settings, although other inflammatory cytokine levels including IL-1 and IL-6 were low (data not shown), significant production of TNF-α was observed. We do not clearly know the source of TNF-α in the tumor at this time, and that our *in vitro* data only suggest that the stroma is the primary source.

As we expected, TNF-α enabled MSCs to adhere to endothelial cells through induction of the expression of adhesion molecules, including VCAM-1 and VLA-4. It is generally considered that VCAM-1 on activated endothelium interacts with the VLA-4 on the leukocyte in the model of leukocyte–endothelial cell adhesion. At first, we speculated that VLA-4 on MSCs plays the same important role as leukocytes. Although both VCAM-1 and VLA-4 on endothelium were efficiently induced by TNF-α stimulation, TNF-α–induced expression of VCAM-1 on MSCs is much stronger than that of VLA-4. Furthermore, MSC–EC adhesion was more effectively inhibited by anti-VCAM-1 antibody as compared with the anti-VLA-4 antibody. On the basis of these results, although VLA-4 on MSC have also related to the MSC-EC adhesion, we thought that VCAM-1 on MSC has more important implications for this adhesion. Once MSCs circulate in the bloodstream, adhesion to endothelial cells is the first step in accumulation in tumors. TNF-α exerts its biologic functions through activating the NF-κB signaling pathway. NF-κB is a major cell survival signal that is antiapoptotic. MSC accumulation was significantly decreased through parthenolide inhibition of NF-κB activity. Although several studies have shown that mitogen-activated protein kinase (MAPK) phosphorylation by growth factors are involved in MSC migration (16, 17), parthenolide did not inhibit MAPK phosphorylation (data not shown). Therefore, at least parthenolide treatment did not affect in migration ability of

Published OnlineFirst October 12, 2012; DOI: 10.1158/0008-5472.CAN-12-0088

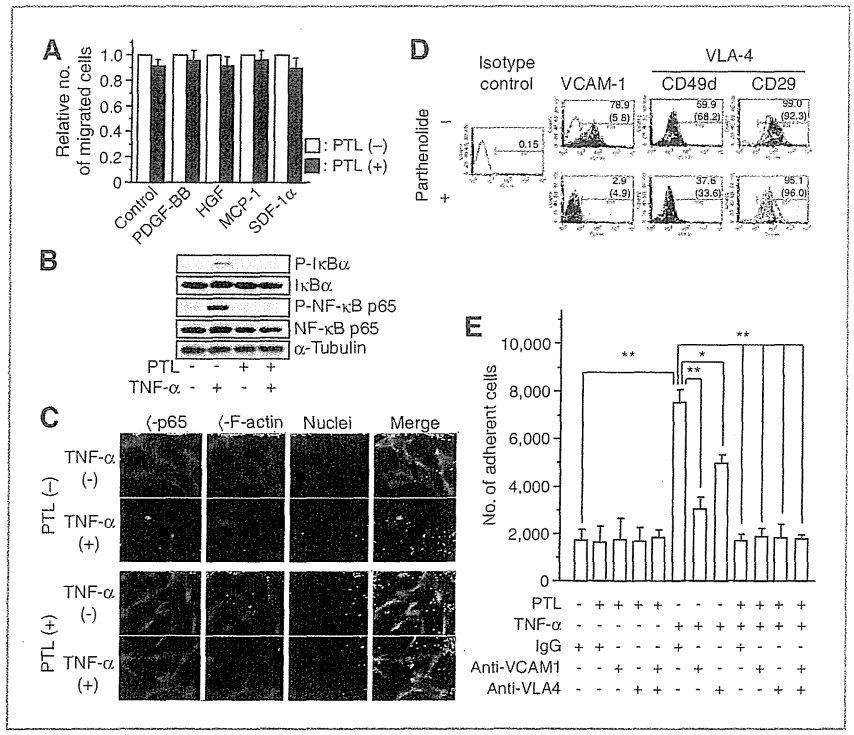

Figure 4. Effect of parthenolide (PTL) on MSC migration and adhesion. A, serum-starved and parthenolide-treated MSCs were added to the upper wells and serum-free medium supplemented with PDGF-BB (10 ng/mL), HGF (30 ng/mL), MCP-1 (100 ng/mL), or SDF-1α (150 ng/mL) was added to the lower wells. Treatment with medium alone (DMEM/F-12) was a negative control and treatment with 30% FBS was the positive control. Values are expressed by relative number of cells compared with respective controls (without pretreatment with parthenolide). B, to assess the inhibitory effect of parthenolide on NF-κB phosphorylation, parthenolide-treated MSCs were stimulated with recombinat TNF-α for 3 minutes, and cellular extracts were prepared for Western blotting. C, to monitor the inhibitory effect of parthenolide on NF-κB activation, immunofluorescent analysis of NF-κB p65 nuclear translocation was conducted as described in Materials and Methods with an Alexa Fluor 488–conjugated specific antibody (green). Actin filaments were labeled with Alexa Fluor 546–conjugated phalloidin (red); nuclei were stained with DRAQ-5 dye (blue). Objective magnification, ×40. D, effect of parthenolide treatment on TNF-α–induced expression of adhesion molecules was analyzed by flow cytometry. Parthenolide-treated MSCs were cultured with TNF-α (10 ng/mL) for 6 hours. Cells were labeled with FITC-conjugated antibodies and analyzed by flow cytometry (filled histogram). Rat isotype antibodies IgG1 and IgG2a served as respective controls (open histograms). Values represent the percentage of positive cells after TNF-α stimulation, and values in parentheses represent the percentage of positive cells without TNF-α stimulation. E, MSCs (1×10^4) were added to endothelial cells that had been cultured to confluence on fibronectin-coated 96-well plates. MSCs and endothelial cells were pretreated with the following substances: parthenolide (5 μmol/L), TNF-α (10 ng/mL), anti-VCAM-1, VLA-4 (10 μg/mL), or isotype control IgG. Values are expressed as mean ± SD ($n = 6$). *, $P < 0.05$ and **, $P < 0.01$.

MSCs toward growth factors from tumors in this experimental settings. Nevertheless, MSC accumulation was significantly decreased through parthenolide inhibition of NF-κB activity. We did not show histologic evidence in the experiments using parthenolide. However, we show that parthenolide does not inhibit luciferase activity *in vitro* (and thus does not seem to be toxic), and that therefore the effect observed *in vivo* should be an effect on recruitment. Although we focused on the function of TNF-α in this study, other inflammatory cytokines including IL-1β and IFN-γ also have ability to induce VCAM-1 expression in target cells (18), and may be involved in MSC accumulation.

TNF-α is a major inflammatory cytokine that plays important roles in diverse cellular events, such as cell survival, proliferation, differentiation, and death. Numerous reports have shown that TNF-α levels in serum are increased in patients with cancer (19, 20), and TNF-α is also related closely to the tumor progression including metastasis. For example, TNF-α intensely induces IL-6 and MCP-1 from cancer-associated fibroblasts and normal fibroblastic cells and has indirect influences on generation of prometastatic microenvironment (21). Furthermore, TNF-α is also released in cardiac infarction, during acute coronary syndromes, and in chronic heart failure; MSCs also accumulate at the site of cardiac infarction (22, 23). These results indicated that proinflammatory cytokines promote homing of stem cells in the heart and that these cytokines have a positive effect on cardiac regeneration. Therefore, activation with TNF-α is one of the critically important steps for MSC accumulation. Moreover, MSC-based tissue-targeted strategies may be adapted for various inflammatory diseases.

In MSC-based cancer-targeted gene therapies, it is thought that therapeutic efficacy is directly linked with accumulation efficiency of MSCs at tumor sites. Our results suggested that combination use of NF-κB inhibitors, including bortezomib, or TNF-α blocking agents, such as infliximab, reduces the

Published OnlineFirst October 12, 2012; DOI: 10.1158/0008-5472.CAN-12-0088

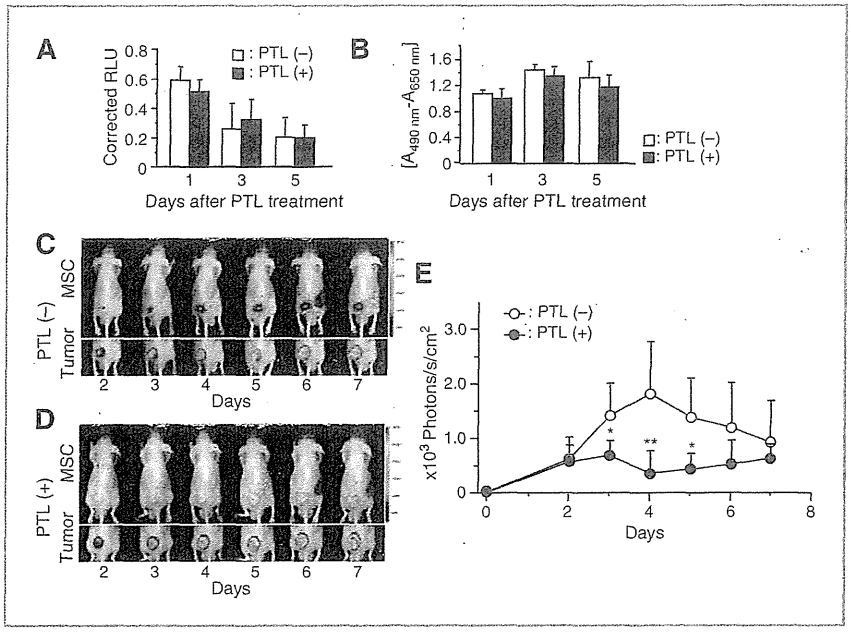

Figure 5. *In vivo* imaging of NF-κB–suppressed MSC accumulation at tumor sites. A, luciferase-expressing MSCs were cultured with parthenolide for 6 hours and luciferase assays were periodically conducted. Values are expressed as mean ± SD ($n = 4$ each). RLU, relative light unit. B, cell viability of parthenolide (PTL)-treated luciferase-expressing MSCs was also examined by XTT assays. Values are expressed as mean ± SD ($n = 4$ each). C, luciferase-expressing MSCs without parthenolide treatment were injected into tumor-bearing mice through the left ventricular cavity and IVIS imaging was periodically conducted. Each data shown are from 1 representative experiment of 8 carried out. D, luciferase-expressing MSCs with parthenolide treatment were injected into tumor-bearing mice and IVIS imaging was periodically conducted. Imaging was conducted as described earlier. Each data shown are from 1 representative experiment of 8 carried out. E, bioluminescent intensity at tumor sites was quantified using analysis software. The data are expressed as mean ± SD ($n = 8$ each). *, $P < 0.05$; **, $P < 0.01$ compared with a group of parthenolide (−) at the same time.

therapeutic efficacy of gene-modified MSCs due to inhibition of the accumulation steps. In contrast, tumor-specific TNF-α–inducing agents would be useful in enhancing therapeutic efficacy, thus further research is required in identifying such agents to more effective therapeutic strategies.

In conclusion, the present study shows that NF-κB activation through TNF-α stimulation and VCAM-1/VLA-4–mediated MSC-EC adhesion may be an important element in MSC accumulation. Although MSCs are useful as cellular vehicles for cancer-targeted gene therapy, past studies have shown that increased MSC accumulation is needed to enhance therapeutic efficacy. Thus, methodology for the enhancement of MSC accumulation should be developed and our findings suggest a solution.

Disclosure of Potential Conflicts of Interest

No potential conflicts of interest were disclosed.

Authors' Contributions

Conception and design: R. Uchibori, H. Mizukami, K. Ozawa
Development of methodology: M. Urabe
Acquisition of data (provided animals, acquired and managed patients, provided facilities, etc.): R. Uchibori
Analysis and interpretation of data (e.g., statistical analysis, biostatistics, computational analysis): R. Uchibori, H. Mizukami, A. Kume
Writing, review, and/or revision of the manuscript: R. Uchibori, M. Urabe, A. Kume
Administrative, technical, or material support (i.e., reporting or organizing data, constructing databases): T. Tsukahara, H. Mizuguchi, Y. Saga, K. Ozawa
Study supervision: M. Urabe, A. Kume, K. Ozawa

Acknowledgments

The authors thank Miyoko Mitsu for her encouragement and technical support.

Grant Support

This work was supported by Grant-in-Aid for Scientific Research (KAKENHI) from the Ministry of Education, Culture, Sports, Science and Technology (21390296 to K. Ozawa), and The Research Award to Jichi Medical School Graduate Student (to R. Uchibori).

The costs of publication of this article were defrayed in part by the payment of page charges. This article must therefore be hereby marked *advertisement* in accordance with 18 U.S.C. Section 1734 solely to indicate this fact.

Received January 13, 2012; revised August 30, 2012; accepted September 11, 2012; published OnlineFirst October 12, 2012.

References

1. Studeny M, Marini FC, Champlin RE, Zompetta C, Fidler IJ, Andreeff M. Bone marrow-derived mesenchymal stem cells as vehicles for interferon-beta delivery into tumors. Cancer Res 2002;62:3603–8.

Published OnlineFirst October 12, 2012; DOI: 10.1158/0008-5472.CAN-12-0088

2. Studeny M, Marini FC, Dembinski JL, Zompetta C, Cabreira-Hansen M, Bekele BN, et al. Mesenchymal stem cells: potential precursors for tumor stroma and targeted-delivery vehicles for anticancer agents. J Natl Cancer Inst 2004;96:1593–603.
3. Nakamizo A, Marini F, Amano T, Khan A, Studeny M, Gumin J, et al. Human bone marrow-derived mesenchymal stem cells in the treatment of gliomas. Cancer Res 2005;65:3307–18.
4. Chen X, Lin X, Zhao J, Shi W, Zhang H, Wang Y, et al. A tumor-selective biotherapy with prolonged impact on established metastases based on cytokine gene-engineered MSCs. Mol Ther 2008;16:749–56.
5. Xin H, Kanehira M, Mizuguchi H, Hayakawa T, Kikuchi T, Nukiwa T, et al. Targeted delivery of CX3CL1 to multiple lung tumors by mesenchymal stem cells. Stem Cells 2007;25:1618–26.
6. Uchibori R, Okada T, Ito T, Urabe M, Mizukami H, Kume A, et al. Retroviral vector-producing mesenchymal stem cells for targeted suicide cancer gene therapy. J Gene Med 2009;11:373–81.
7. Dwyer RM, Potter-Beirne SM, Harrington KA, Lowery AJ, Hennessy E, Murphy JM, et al. Monocyte chemotactic protein-1 secreted by primary breast tumors stimulates migration of mesenchymal stem cells. Clin Cancer Res 2007;13:5020–7.
8. Mizuguchi H, Kay MA. Efficient construction of a recombinant adenovirus vector by an improved *in vitro* ligation method. Hum Gene Ther 1998;9:2577–83.
9. Mizuguchi H, Kay MA. A simple method for constructing E1- and E1/E4-deleted recombinant adenoviral vectors. Hum Gene Ther 1999; 10:2013–7.
10. Koizumi N, Mizuguchi H, Utoguchi N, Watanabe Y, Hayakawa T. Generation of fiber-modified adenovirus vectors containing heterologous peptides in both the HI loop and C terminus of the fiber knob. J Gene Med 2003;5:267–76.
11. Mittereder N, March KL, Trapnell BC. Evaluation of the concentration and bioactivity of adenovirus vectors for gene therapy. J Virol 1996;70:7498–509.
12. Coussens LM, Werb Z. Inflammation and cancer. Nature 2002;420: 860–7.
13. Honczarenko M, Le Y, Swierkowski M, Ghiran I, Glodek AM, Silberstein LE. Human bone marrow stromal cells express a distinct set of biologically functional chemokine receptors. Stem Cells 2006;24: 1030–41.
14. Rüster B, Göttig S, Ludwig RJ, Bistrian R, Müller S, Seifried E, et al. Mesenchymal stem cells display coordinated rolling and adhesion behavior on endothelial cells. Blood 2006;108:3938–44.
15. Butcher EC. Leukocyte-endothelial cell recognition: three (or more) steps to specificity and diversity. Cell 1991;67:1033–6.
16. Coffelt SB, Marini FC, Watson K, Zwezdaryk KJ, Dembinski JL, LaMarcad HL, et al. The pro-inflammatory peptide LL-37 promotes ovarian tumor progression through recruitment of multipotent mesenchymal stromal cells. Proc Natl Acad Sci U S A 2009; 106:3806–11.
17. Zhang A, Wang Y, Ye Z, Xie H, Zhou L, Zheng S. Mechanism of TNF-α-induced migration and hepatocyte growth factor production in human mesenchymal stem cells. J Cell Biochem 2010;111: 469–75.
18. Hosokawa Y, Hosokawa I, Ozaki K, Nakae H, Matsuo T. Cytokines differentially regulate ICAM-1 and VCAM-1 expression on human gingival fibroblasts. Clin Exp Immunol 2006;144:494–502.
19. Ferrajoli A, Keating MJ, Manshouri T, Giles FJ, Dey A, Estrov Z, et al. The clinical significance of tumor necrosis factor-alpha plasma level in patients having chronic lymphocytic leukemia. Blood 2002;100: 1215–9.
20. Ahmed MI, Salahy EE, Fayed ST, El-Hefnawy NG, Khalifa A. Human papillomavirus infection among Egyptian females with cervical carcinoma: relationship to spontaneous apoptosis and TNF-alpha. Clin Biochem 2001;34:491–8.
21. Mueller L, von Seggern L, Schumacher J, Goumas F, Wilms C, Braun F, et al. TNF-alpha similarly induces IL-6 and MCP-1 in fibroblasts from colorectal liver metastases and normal liver fibroblasts. Biochem Biophys Res Commun 2010;397:586–91.
22. Shake JG, Gruber PJ, Baumgartner WA, Senechal G, Meyers J, Redmond JM, et al. Mesenchymal stem cell implantation in a swine myocardial infarct model: engraftment and functional effects. Ann Thorac Surg 2002;73:1919–25.
23. Pittenger MF, Martin BJ. Mesenchymal stem cells and their potential as cardiac therapeutics. Circ Res 2004;95:9–20.

The Endothelial Antigen ESAM Monitors Hematopoietic Stem Cell Status between Quiescence and Self-Renewal

Takao Sudo,* Takafumi Yokota,* Kenji Oritani,* Yusuke Satoh,* Tatsuki Sugiyama,† Tatsuro Ishida,‡ Hirohiko Shibayama,* Sachiko Ezoe,* Natsuko Fujita,* Hirokazu Tanaka,*,[1] Tetsuo Maeda,* Takashi Nagasawa,† and Yuzuru Kanakura*

Whereas most hematopoietic stem cells (HSC) are quiescent in homeostasis, they actively proliferate in response to bone marrow (BM) injury. Signals from the BM microenvironment are thought to promote entry of HSC into the cell cycle. However, it has been cumbersome to assess cycle status of viable HSC and thus explore unique features associated with division. In this study, we show that expression of endothelial cell-selective adhesion molecule (ESAM) can be a powerful indicator of HSC activation. ESAM levels clearly mirrored the shift of HSC between quiescence and activation, and it was prominent in comparison with other HSC-related Ags. ESAM^{hi} HSC were actively dividing, but had surprisingly high long-term reconstituting capacity. Immunohistochemical analyses showed that most ESAM^{hi} HSC were located near vascular endothelium in the BM after 5-fluorouracil treatment. To determine the importance of ESAM in the process of BM recovery, ESAM knockout mice were treated with 5-fluorouracil and their hematopoietic reconstruction was examined. The ESAM deficiency caused severe and prolonged BM suppression, suggesting that ESAM is functionally indispensable for HSC to re-establish homeostatic hematopoiesis. With respect to intracellular regulators, NF-κB and topoisomerase II levels correlated with the ESAM upregulation. Thus, our data demonstrate that the intensity of ESAM expression is useful to trace activated HSC and to understand molecular events involved in stem cell states. *The Journal of Immunology*, **2012, 189: 200–210.**

Hematopoietic stem cells (HSC) are characterized as being extensively self-renewing as well as multipotent. Distinction of HSC from differentiating cells is essential for understanding the essence of "stemness." Many groups have identified HSC-related Ags, and those markers have made it possible to sort long-term reconstituting HSC (LT-HSC) with high purity. For example, at least one in three lineage (Lin)$^-$c-Kit^{hi}Sca-1$^+$CD34$^-$Flk2/Flt3$^-$CD150$^+$CD48$^-$ fraction cells in adult mouse bone marrow (BM) can be transplanted (1–3). Recent studies using a BrdU-retaining method and/or a histone 2B-GFP transgene have shown that the long-term reconstituting activity of the adult mouse BM is sustained mostly in very quiescent HSC that divide only five to six times during the adult period (4, 5). However, even the highly purified LT-HSC fraction is heterogeneous with respect to cell cycle status (4, 5).

The cell cycle status and differentiating behavior of HSC are known to fluctuate according to physiological circumstances. During fetal and early postnatal periods, development of the hematopoietic system is essential in supporting the rapid growth of organisms and the explosive expansion of all blood lineages. Indeed, numbers of HSC increase ~40-fold in the fetal liver between embryonic days 12 and 16 (6). Alternatively, upon reaching adulthood, HSC become quiescent and evade exhaustion or mutation to maintain hematopoiesis throughout life (7). Although the quiescent HSC divide at an extremely low rate during homeostasis, they are rapidly activated to proliferate in response to BM injury or by G-CSF stimulation (5). Interestingly, after re-establishment of homeostasis, the activated HSC can return to quiescence. Distinguishing LT-HSC from differentiating progenitors becomes complicated by BM injury because the expression pattern of HSC-related Ags is dramatically influenced (8). Molecular crosstalk between HSC and the BM microenvironment, also known as "HSC niche," is likely to control the balance of HSC quiescence and activity (9, 10), but precise mechanisms regulating HSC status remain largely unknown. If we could selectively isolate active HSC with a set of surface markers, that should yield significant insights regarding HSC biology and HSC applications for clinical purposes. Furthermore, information about cell surface Ags that mirror HSC states would be invaluable for understanding the relationship between HSC and their niches.

Endothelial cell-selective adhesion molecule (ESAM), which is an Ig superfamily protein, was originally identified as an endothelial specific molecule mediating cell–cell adhesion through homophilic interactions (11, 12). ESAM proteins colocalize with cadherins and catenins in cell–cell junctions of vascular endothelium. ESAM deficiency in endothelial tight junctions disturbs neutrophil extravasation to inflamed tissues by reduction of acti-

*Department of Hematology and Oncology, Osaka University Graduate School of Medicine, Suita, Osaka 565-0871, Japan; †Department of Immunobiology and Hematology, Institute for Frontier Medical Sciences, Kyoto University, Kyoto 606-8507, Japan; and ‡Division of Cardiovascular Medicine, Department of Internal Medicine, Kobe University Graduate School of Medicine, Kobe, Hyogo 650-0017, Japan

[1]Current address: Division of Hematology, Department of Internal Medicine, Kinki University School of Medicine, Osaka, Japan.

Received for publication January 6, 2012. Accepted for publication May 2, 2012.

This work was supported in part by a grant from the Mitsubishi Pharma Research Foundation.

Address correspondence and reprint requests to Dr. Takafumi Yokota, Department of Hematology and Oncology, Osaka University Graduate School of Medicine, C9, 2-2 Yamadaoka, Suita, Osaka 565-0871, Japan. E-mail address: yokotat@bldon.med.osaka-u.ac.jp

The online version of this article contains supplemental material.

Abbreviations used in this article: BM, bone marrow; E, embryonic day; ESAM, endothelial cell-selective adhesion molecule; 5-FU, 5-fluorouracil; HSC, hematopoietic stem cell; KO, knockout; Lin, lineage; LSK, Lin$^-$Sca1$^+$c-Kit$^+$; LT-HSC, long-term reconstituting hematopoietic stem cell; ROS, reactive oxygen species; RU, repopulating unit; SAv, streptavidin; TR, Texas Red; WT, wild-type.

www.jimmunol.org/cgi/doi/10.4049/jimmunol.1200056

vated Rho proteins (13). The deficiency also increases vascular permeability of the renal glomeruli, resulting in urinary albumin elevation (14). Additionally, it has been shown that ESAM is also expressed on megakaryocytes and platelets (12), where it is involved in the regulation of thrombus formation (15).

Our recent study revealed that ESAM is also useful as an HSC marker (16). Hematopoietic and endothelial cells are both derived from mesoderm and share many features with respect to cell surface molecules. Some endothelial-related markers are known to become undetectable on HSC in adult BM, but they are upregulated upon hematopoietic reconstruction after treatment with myelosuppressive drugs or irradiation (17). Although ESAM marks LT-HSC throughout adult life, we observed that there are some age-related changes regarding the intensity of expression (16). We have now studied changes in ESAM levels on adult HSC following BM stress. Our data show that ESAM represents a powerful tool for monitoring the fluctuation between quiescence and self-renewal of the adult BM HSC. Additionally, our experiments using ESAM knockout (KO) mice suggest that ESAM is indispensable for normal hematopoietic recovery after BM injury.

Materials and Methods

Mice

Wild-type (WT) C57BL/6, BALB/c, and FVB mice were obtained from CLEA Japan (Shizuoka, Japan). The congenic C57BL/6 strain (C57BL/6SJL; CD45.1 alloantigen) was purchased from The Jackson Laboratory (Bar Harbor, ME) and used for transplantation experiments. ESAM KO mice were developed by Dr. T. Ishida (Kobe University, Kobe, Japan) as previously reported (18). Mating of heterozygous male and female mice was routinely performed to generate homozygous ESAM KO mice. Three types of PCR primers were used to genotype ESAM KO mice as documented previously (19). All mice used in this article were 8–12 wk old. Animal studies were performed with the approval of the Institutional Review Board of Osaka University.

Abs and reagents

5-Fluorouracil (5-FU) was purchased from Kyowa-Hakko Kirin (Tokyo, Japan). Purified anti-Ly6G and Ly6C/Gr1 (RB6-8C5) mAb, PE-conjugated anti-CD3e (145-2C11), CD45.1 (A20), and CD48 (HM48-1) mAbs, FITC-conjugated and allophycocyanin-conjugated anti-CD11b/Mac1 (M1/70), Ly6G and Ly6C/Gr1 (RB6-8C5), CD45R/B220 (RA3-6B2), Ter119, CD3e (145-2C11), and CD8a (53-6.7) mAbs, allophycocyanin-conjugated anti-CD117/c-Kit (2B8) mAb, PE-Cy7–conjugated anti-Sca1 (Ly6A/E; D7) mAb, biotinylated anti-Sca1 (E13-161.7) mAb, PerCP-Cy5.5–conjugated anti-CD45.2 (104) mAb, and Alexa Fluor 647-conjugated anti-CD19 (1D3) mAb, streptavidin (SAv)-PE, and SAv-PE-Texas Red (TR) were purchased from BD Pharmingen (San Diego, CA). Purified anti-CD3 (17A2), Mac1 (M1/70), and Ter119 mAbs, and PE-conjugated anti-CD105/endoglin (MJ7/18), CD31/PECAM-1 (390), Tie2 (TEK4), and CD135/Flt3 (A2F10) mAbs were purchased from eBioscience (San Diego, CA). PE-conjugated and allophycocyanin-conjugated anti-CD150 (TC15-12F12.2) mAbs and PerCP-Cy5.5–conjugated anti–CD117/c-Kit (2B8) mAb were purchased from BioLegend (San Diego, CA). Cy3-conjugated goat anti-rat IgG Ab was purchased from Jackson ImmunoResearch Laboratories (West Grove, PA). Streptavidin-Alexa Fluor 647 was purchased from Invitrogen (Carlsbad, CA). FITC-conjugated Ki67 (M-19) mAb was purchased from Santa Cruz Biotechnology (Santa Cruz, CA). A rat anti-mouse ESAM (1G8) mAb, which was originally developed and supplied by Drs. S. Butz and D. Vestweber (Max Planck Institute, Muenster, Germany), was purchased from BioLegend. The Ab was biotinylated in our hands using Sulfo-NHS-LC-Biotin (Thermo Fisher Scientific, Rockford, IL). Bortezomib (Velcade) was purchased from Janssen (Tokyo, Japan). ICRF-193 was purchased from Funakoshi (Tokyo, Japan). TaqMan FAM dye-labeled MGB probe sets for ESAM and GAPDH were purchased from Applied Biosystems (Foster City, CA).

Flow cytometry

Cells were obtained from adult mouse tissues indicated in each experiment and first incubated with a rat anti-mouse FcRII/III Ab (2.4G2) to block nonspecific Ab binding via FcR. Then, the cells were stained with the indicated Abs. Lin Abs contain anti-Mac1, Gr1, CD3e, CD45R/B220, and Ter119 Abs for analysis of untreated control mice, and Gr1, CD3e, CD45R/B220, and Ter119 for 5-FU–treated mice, as the level of Mac1 on HSC revives after a 5-FU treatment. A biotinylated anti-ESAM Ab was developed with SAv-PE or SAv-PE-TR. Flow cytometry analyses were performed with FACSAria or FACSCanto (BD Biosciences). The data analyses were done with FlowJo software (Tree Star, San Carlos, CA).

Quantitative real-time PCR

RNA samples from $Lin^-Sca1^+c\text{-}Kit^+$ (LSK) cells were isolated using a PureLink RNA Mini kit (Invitrogen). Reverse transcription reactions were performed using a high-capacity RNA-to-cDNA kit (Applied Biosystems). Relative expression levels of ESAM were evaluated according to TaqMan gene expression assay protocol (Applied Biosystems). Taqman FAM dye-labeled MGB probe sets for ESAM and GAPDH were purchased from Applied Biosystems. Reactions were run on the 7900HT Fast real-time PCR system (Applied Biosystems). The data were analyzed using SDS 2.3 software (Applied Biosystems).

Cell cycle analyses

Mice were given a single 5-FU injection and analyzed. BrdU was i.p. administered 12 h before analyses. BM cells were stained with biotynilated anti-ESAM, PE-Cy7-anti-Sca1, and allophycocyanin-anti–c-Kit Abs, followed by SAv-PE. The stained cells were then fixed, permeabilized, and incubated with DNase to expose incorporated BrdU by using a BrdU flow kit (BD Pharmingen). Subsequently, the cells were stained with FITC-anti-BrdU Ab for 30 min at room temperature and resuspended with staining medium containing 7-aminoactinomycin D. For another staining set, the cells were incubated with 2 μg/ml Hoechst 33342 (Sigma-Aldrich, St. Louis, MO) and FITC-anti-Ki67 Ab for 30 min at room temperature. Cell cycle statuses were analyzed by FACSAria (BD Biosciences).

Cell isolation

BM cells obtained from femora and tibiae of adult mice were first incubated with purified anti-Lin Abs, followed by goat anti-rat IgG microbeads (Miltenyi Biotec). After Lin^+ cell depletion, the Lin^--enriched cells were stained with FITC-anti-Lin Abs in combination with PE-Cy7-anti-Sca1, allophycocyanin-anti–c-Kit, and biotinylated anti-ESAM Abs. Subsequent to staining with SAv-PE, $ESAM^{lo}$ and $ESAM^{hi}$ LSK cells were sorted with FACSAria. The purity of the sorted cells was routinely confirmed by using a part of each sorted population to be >97%.

Methylcellulose cultures

C57BL/6 mice were treated with single i.v. 5-FU (150 mg/kg). Five days after treatment, mice were killed and $ESAM^{lo}$ or $ESAM^{hi}$ LSK cells of BM were sorted and subjected to methylcellulose colony formation assays. Two hundred cells of each sorted fraction were cultured in IMDM-based methylcellulose medium supplemented with 50 ng/ml recombinant murine stem cell factor, 10 ng/ml recombinant murine IL-3, 10 ng/ml recombinant human IL-6, and 3 U /ml recombinant human erythropoietin (Methocult GF 3434; StemCell Technologies, Vancouver, BC, Canada). After 9–10 d, colonies were enumerated and classified as CFU-GM, CFU-M, BFU-E, or CFU-Mix according to shape and color under an inverted microscope.

Competitive repopulation assay

Ly5 congenic mice were used for competitive repopulation assays. Two thousand $ESAM^{lo}$ LSK or $ESAM^{hi}$ LSK cells sorted from C57BL/6-Ly5.1 (CD45.1) mice were mixed with 2×10^5 unfractionated adult BM cells obtained from WT C57BL/6-Ly5.2 (CD45.2) mice and were transplanted into C57BL/6-Ly5.2 mice irradiated at a dose of 8.5 Gy. Peripheral blood analyses were performed at 4-wk intervals after transplantation. Sixteen weeks after transplantation, all recipients were killed and BM cells were collected. BM cells were stained with FITC-anti-Mac1, PE-anti-CD3e, Alexa Fluor 647-anti-CD19, PerCP-Cy5.5-anti-CD45.2, and PE-Cy7-anti-CD45.1 Abs to analyze the donor-derived chimerism and each lineage differentiation, and they were simultaneously stained with FITC-anti-Lin, PE-anti-CD45.1, PerCP-Cy5.5-anti-CD45.2, PE-Cy7-anti-Sca1, and allophycocyanin-anti–c-Kit, and biotinylated anti-ESAM Abs, followed by SAv-PE-TR to evaluate ESAM level of LSK fraction. The repopulating unit (RU) was calculated as follows: RU = [(% donor-derived cells) × (number of competitor cells/10^5)]/(% competitor-derived cells) (20). The total number of RU per BM was obtained by multiplying the number of RU per 2000 test cells by the number of $ESAM^{lo}$ LSK or $ESAM^{hi}$ LSK cells per BM (two femora and two tibiae) divided by 2000. For the second transplantation, two hundred $CD45.1^+$ LSK cells sorted from primary recipient mice were mixed with 1×10^5 unfractionated BM cells obtained

from WT C57BL/6-Ly5.2 (CD45.2) mice and were transplanted into irradiated C57BL/6-Ly5.2 mice. Sixteen weeks after transplantation, the contribution of CD45.1 cells to the hematopoietic reconstitution was evaluated.

Immunohistochemical analyses

Immunohistochemical staining was performed as described previously (21). In brief, bone samples were fixed in 4% paraformaldehyde and equilibrated in 30% sucrose/PBS. Fixed samples were embedded in OCT medium (Sakura Finetek, Tokyo, Japan) and frozen in cooled hexane. Sections of undecalcified femoral bone were generated via Kawamoto's film method (Cryofilm transfer kit; Leica Microsystems). The 8-μm-thick cryostat sections were first blocked with 5% FCS/PBS and then stained with mAbs. The following Abs were used for immunostaining: FITC-conjugated mAbs against Gr1, B220, CD3e, CD8, and Ter119; biotinylated mAb against Sca1; and purified mAb against ESAM. For secondary Ab, Cy3-conjugated donkey anti-rat IgG Ab was used. Biotinylated Ab was visualized with SAv-Alexa Fluor 647. The nuclei of cells were labeled with DAPI (Dojindo, Kumamoto, Japan). The sections were mounted with PermaFluor (Thermo Fisher Scientific), and confocal microscopic analyses were performed with an LSM 510 META (Carl Zeiss, Oberkochen, Germany). Image analyses were performed using an LSM image browser (Carl Zeiss).

Luciferase assays

Promoter sequences of ESAM gene were searched with Genetyx version 9 (Genetyx, Tokyo, Japan). Segments of ESAM genes were amplified by PCR and inserted in pGL3 basic vector (Promega, Madison, WI). Luciferase assays were performed using the endothelial bEnd3 cell line. The cells were seeded in 3.5-cm dishes, and 24 h later each pGL3-promoter construct and pRL-CMV encoding the *Renilla* luciferase gene were transfected into the cells by Lipofectamine. Each culture medium was changed 24 h after transfection. Luciferase assays with use of a luminometer were carried out 48 h after transfection.

Statistical analyses

Statistical analyses of chimerism status were carried out with Mann–Whitney *U* tests, and other analyses were conducted with standard Student *t* tests. Error bars used throughout indicate SD of the mean.

Results

BM injury upregulates ESAM expression on HSC

We have reported that ESAM is a durable marker for fetal and adult HSC (16). Levels decline in early postnatal life and become high again with age (16). Several Ags, including Mac1 and CD34, are known to be downregulated when fetal HSC switch to quiescent adult ones, but they emerge again on HSC as activation-related changes after myelosuppression (8, 17). We monitored ESAM expression levels in HSC-enriched fraction of adult C57BL/6 BM after a single 5-FU treatment (150 mg/kg) by flow cytometry (Fig. 1A). As shown in a previous report (8), 5-FU injection caused significant downregulation of c-Kit expression on Lin^- cells (Supplemental Fig. 1). In the same report, HSC could be enriched in the $Lin^-Sca1^+c\text{-}Kit^{dull}$ fraction after 5-FU treatment (8). Therefore, in our experiments, we applied an enlarged LSK gate covering the $c\text{-}Kit^{dull}$ HSC.

We observed remarkable increases in ESAM levels in HSC-enriched fractions from days 2–9 after a 5-FU injection (Fig. 1A). Indeed, the mean fluorescence intensity of ESAM expression on LSK increased by 11-fold in 5 d after a single 5-FU injection, compared with untreated control mice. More than 70% of LSK cells on day 5 expressed high amounts of ESAM (fluorescence intensities >10-fold the maximum level of isotype controls). After reaching peak values around days 5–6, ESAM levels gradually decreased and returned to steady-state levels by day 12.

$ESAM^{hi}$ cells formed a dominant population in the LSK fraction and logarithmically increased from day 3 to 9 in parallel with hematopoietic recovery (Fig. 1B). Quantitative real-time PCR showed gradual increases of ESAM transcripts in the LSK fraction after 5-FU treatment (Fig. 1C), suggesting that something associated with BM injury activates ESAM expression at the gene transcription level. Sublethal total body irradiation caused essentially the same change on the HSC fraction (data not shown). We evaluated ESAM levels of BM HSC fractions in BALB/c and FVB strains other than C57BL/6 mice. Expression of ESAM was also upregulated after 5-FU treatment in the $CD150^+Lin^-c\text{-}Kit^+Flt3^-$ fraction (Fig. 1D). These results suggested that BM injury upregulates ESAM levels on HSC.

Upregulation of ESAM on HSC after BM injury in comparison with other endothelial markers

Recent studies have shown that the gate of $CD150^+CD48^-$ is useful to enrich for LT-HSC activity in various contexts, from aged BM, mobilized splenocytes, or reconstituted mouse BM (1, 22). Therefore, we evaluated whether ESAM expression patterns were shared with those of SLAM family markers on adult C57BL/6 LSK cells before and after 5-FU injection. In the homeostatic BM LSK, $CD150^+CD48^-$ cells were only detectable among the $ESAM^+$ population and the percentage was higher in $ESAM^{hi}$ than $ESAM^{lo}$ (Fig. 2A, *left panels*). After 5-FU injection, more than half of LSK cells were found in the $CD150^+$ fraction, whose levels of ESAM were clearly upregulated. Additionally, percentages of the population that were $CD150^+CD48^-$ were also higher in $ESAM^{hi}$ than $ESAM^{lo}$ categories (Fig. 2A, *right panels*). With respect to mobilized LSK cells, we also detected increases of $ESAM^{hi}CD150^+$ cells in spleens and peripheral blood after day 7 from a 5-FU injection (Supplemental Fig. 2).

HSC are known to share various surface Ags with endothelial cells. We next evaluated how ESAM expression correlates with other endothelial-related HSC markers. The $ESAM^+$ LSK population in the homeostatic BM was found in $CD34^-$, $Tie2^{lo}$ $endoglin^+$, and $CD31/PECAM\text{-}1^{hi}$, which is consistent with the phenotype of adult BM LT-HSC (Fig. 2B). After 5-FU injection, the expression patterns of those markers also changed. Whereas CD34 and Tie2 showed modest increases, endoglin as well as ESAM were clearly upregulated. The CD31/PECAM-1 levels remained unchanged. These results indicate that patterns of several endothelial markers on HSC after BM injury are not homogeneous. Additionally, among the markers, ESAM appeared to be uniquely valuable for monitoring HSC activation.

$ESAM^{hi}$ HSC are actively dividing

Previous studies have proposed that BM HSC in homeostasis are quiescent, a characteristic assumed to protect them from antimetabolites such as 5-FU (4, 5, 23, 24). However, upon their activation by BM injury, it has been hypothesized that HSC move out of their homeostatic niche to proliferate and differentiate (25). To confirm that the $ESAM^{hi}$ HSC in 5-FU–treated mice are actively proliferating, we conducted cell cycle analyses. Although most $ESAM^{lo}$ and $ESAM^{hi}Sca1^+c\text{-}Kit^+$ cells after a 5-FU injection left the G_0 stage and entered into G_1 and $S+G_2+M$, the $ESAM^{hi}$ cells showed even higher percentages entering cell cycle than did the $ESAM^{lo}$ subset (Fig. 3, *upper panels*). Short-term exposure to BrdU marked more cycling cells in the $ESAM^{hi}$ fraction than in the $ESAM^{lo}$ cohort (Fig. 3, *lower panels*). $CD150^+ESAM^{hi}$ LSK cells also showed higher percentages entering cell cycle than did the $CD150^+ESAM^{lo}$ LSK cells (Supplemental Fig. 3A). Based on the fact that total stem cell activity per liver from day 12 to 16 of gestation is higher than that after day 16 (6), we compared ESAM levels in HSC fractions between embryonic day (E)14.5 and E18.5 fetal liver. ESAM levels at E14.5 were 1.9-fold higher than that at E18.5 (Supplemental Fig. 3B). These results suggest that expression of ESAM is associated with rapid division before and after birth.

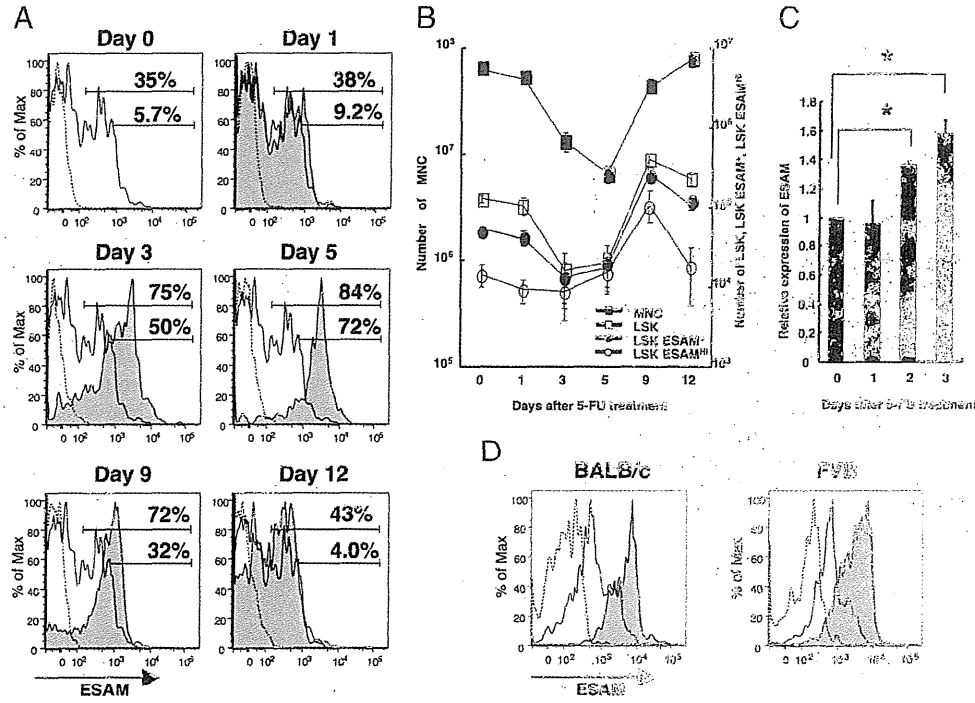

FIGURE 1. ESAM expression is upregulated on LSK cells after 5-FU treatment. (**A**) Flow cytometry analyses were performed with respect to the ESAM expression on murine BM LSK fraction through a single 5-FU (150 mg/kg) treatment. Each panel shows a representative histogram of ESAM level on LSK at days 0 (no treatment control), 1, 3, 5, 9, and 12 after a 5-FU injection. The dashed lines show background levels with an isotype control Ab. The tinted lines show ESAM levels of LSK at the indicated day after a 5-FU injection. The ESAM level of day 0 is added to each panel as an open histogram with a solid line. Upper and lower numbers in each histogram indicate the percentages of $ESAM^+$ and $ESAM^{hi}$ cells, respectively. (**B**) The numbers of total BM mononuclear cells (MNC) (■), LSK cells (□), LSK $ESAM^+$ cells (●), and LSK $ESAM^{hi}$ cells (○) from a pair of femora and tibiae were monitored after a 5-FU injection. Each point summarizes data from five mice. (**C**) Quantitative real-time PCR analyses for ESAM gene expression of LSK cells after 5-FU treatment were performed. Each bar indicates relative expression level against the expression level of day 0 (ESAM/GAPDH). (**D**) ESAM expression levels on the BM $CD150^+Lin^-c\text{-}Kit^+Flt3^-$ fraction of BALB/c and FVB mice were analyzed. The dashed lines and the solid lines show background levels and ESAM levels, respectively, on day 0. The tinted lines show ESAM levels at day 5 after a 5-FU injection (150 mg/kg). Each line of the histogram shows a representative pattern of three mice. $*p < 0.05$.

$ESAM^{hi}$ HSC have enhanced repopulating capacity

Next, we performed functional assessments of the $ESAM^{lo}$ and $ESAM^{hi}$ LSK fractions sorted from 5-FU–treated BM. In methylcellulose cultures, both fractions showed high colony-forming activities. However, whereas the $ESAM^{lo}$ fraction mainly contained committed progenitors, primitive multipotent progenitors, CFU-Mix, were significantly enriched in the $ESAM^{hi}$ fraction (Fig. 4). Additionally, those CFU-Mix cells formed high proliferative potential colonies (data not shown).

To analyze long-term reconstitution capacities in vivo, we transplanted 2000 $CD45.1^+$ $ESAM^{lo}$ or $ESAM^{hi}$ LSK cells sorted from 5-FU–treated mice, with 2×10^5 $CD45.2^+$ competitor BM cells derived from untreated mice, into lethally irradiated $CD45.2^+$ mice (Fig. 5A). Peripheral blood analyses were performed every 4 wk after transplantation, and at any time point, the mice transplanted with $ESAM^{hi}$ LSK cells showed >3-fold higher contributions of $CD45.1^+$ cells to peripheral leukocytes than did the mice transplanted with $ESAM^{lo}$ LSK cells (data not shown). Sixteen weeks after transplantation, all mice were killed and the contribution of donor type cells in BM was evaluated. The mice transplanted with $ESAM^{hi}$ cells gave significant higher levels of donor reconstitution of mononuclear, T, B, and myeloid cells (Fig. 5B). We also evaluated the contribution of $ESAM^{lo}$ and $ESAM^{hi}$ LSK populations by calculating the number of RU per BM (two femora and two tibiae). This revealed that transplanted $ESAM^{hi}$ LSK cells contained more RU per BM than did $ESAM^{lo}$ LSK cells (Fig. 5C). Additionally, recipient BM transplanted with $ESAM^{hi}$ LSK cells showed higher chimerism in the myeloid lineage, whereas $ESAM^{lo}$ LSK cells tended to reconstitute the B lineage more than did the myeloid lineage (Fig. 5D). This observation seemed to be consistent with previous reports showing that long-term reconstituting HSC predominantly contributed to the myeloid lineage (26). It is noteworthy that ESAM levels on $CD45.1^+$ donor-derived LSK cells were identical to the homeostatic level 16 wk after transplantation in the BM that was transplanted with $CD45.1^+ESAM^{hi}$ LSK cells (Fig. 5E). The $CD45.1^+$ LSK cells in the primary recipients serially reconstituted hematopoiesis in secondary $CD45.2^+$ recipients (data not shown). These results suggested that LT-HSC are enriched in the $ESAM^{hi}$ fraction of LSK cells after 5-FU injection.

Most $ESAM^{hi}$ HSC are located around perivascular areas in 5-FU–treated BM

Next, immunohistochemical analyses were conducted to locate the $ESAM^{hi}$ HSC in 5-FU–treated BM. Without treatment, $ESAM^+$ HSC were not easily distinguished because the ESAM levels were not high enough for this type of assessment (Fig. 6A, *left panels*). However, a single 5-FU treatment significantly increased ESAM expression in the HSC-enriched fraction, so that we could discriminate $ESAM^{hi}Lin^-Sca1^+$ HSC from areas with background staining (Fig. 6A). The 5-FU treatment remarkably reduced Lin^+ cells and enlarged sinusoidal vasculature spaces in BM, which favored our ability to locate the activated HSC (Fig. 6A, *right*

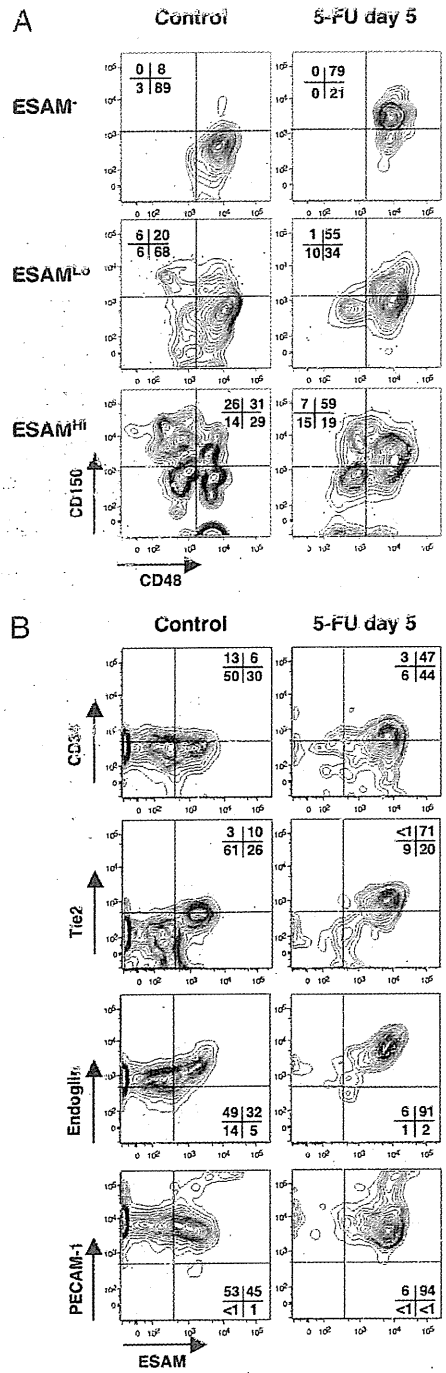

FIGURE 2. HSC express other endothelial Ags, but their patterns do not change in a homogeneous way after 5-FU treatment. (**A**) The expression levels of SLAM family markers (CD48 and CD150) on ESAM$^-$, ESAM^{lo}, and ESAM^{hi} fraction of BM LSK cells were analyzed by flow cytometry. (**B**) The expression of ESAM and endothelial-related Ags (CD34, Tie2, endoglin, and PECAM-1) on BM LSK fraction was analyzed by flow cytometry. (A and B) *Left panels* show the results of homeostatic state mice (control), and *right panels* show those of 5-FU (150 mg/kg)–treated mice (day 5). Numbers in each panel indicate the percentages of each fraction. Each panel shows a representative pattern of three mice.

panels, Supplemental Fig. 4). Note that some ESAM$^+$Sca1$^-$ cells that were not HSC were also found in these sections (Supplemental Fig. 4F). We confirmed by flow cytometry that some types of progenitors expressed low levels of ESAM after 5-FU treatment. Although megakaryocytes that were conspicuous by their morphology and very high ESAM expression distributed around the vasculature, many ESAM^{hi}Lin$^-$Sca1$^+$ cells were also found in the same area, and some of them clustered in perivascular areas (Fig. 6A, *lower right panel*). Indeed, when randomly counted, >80% of the Lin$^-$ESAM^{hi}Sca1$^+$ cells were localized within 20

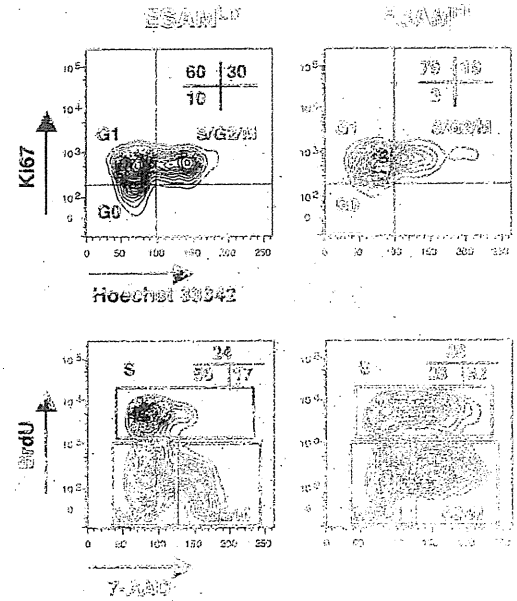

FIGURE 3. ESAM^{hi} HSC in 5-FU–treated mice are dividing. C57BL/6 mice were treated with single i.v. 150 mg/kg 5-FU, and cell cycle analyses of Sca1$^+$c-Kit$^+$ cells in BM were performed at day 5 by flow cytometry. *Upper panels* show Ki67 and Hoechst 33342 staining patterns of ESAM^{lo} or ESAM^{hi} Sca1$^+$c-Kit$^+$ fraction. Numbers in each panel indicate the percentages of G_0, G_1, or S/G_2/M fraction. *Lower panels* show the profile of BrdU and 7-aminoactinomycin D (7-AAD) stainings. BrdU was i.p. administered 12 h before analyses. Numbers in each panel indicate the percentages of G_0/G_1, S, or G_2/M fraction. The data represent three independent trials with similar results.

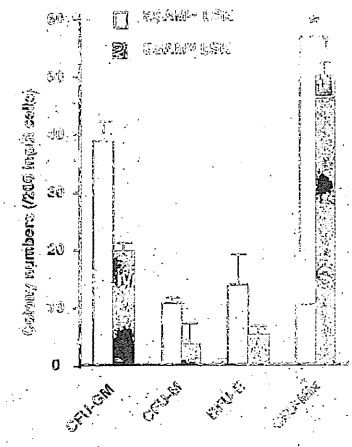

FIGURE 4. Elevated ESAM expression on LSK correlates with CFU activity. C57BL/6 mice treated with single i.v. 150 mg/kg 5-FU were killed 5 d after treatment. ESAM^{lo} or ESAM^{hi} LSK cells of BM were sorted and subjected to methylcellulose colony formation assays. Each dish contained 200 sorted cells, and colony counts were performed 9 d after culture. The bars indicate the number of CFU-GM, CFU-M, BFU-E, or CFU-Mix per one dish from ESAM^{lo} (open bar) or ESAM^{hi} (filled bar) LSK cells. The results are shown as means ± SD. The data are shown as one of two independent experiments that gave similar results. *$p < 0.05$.

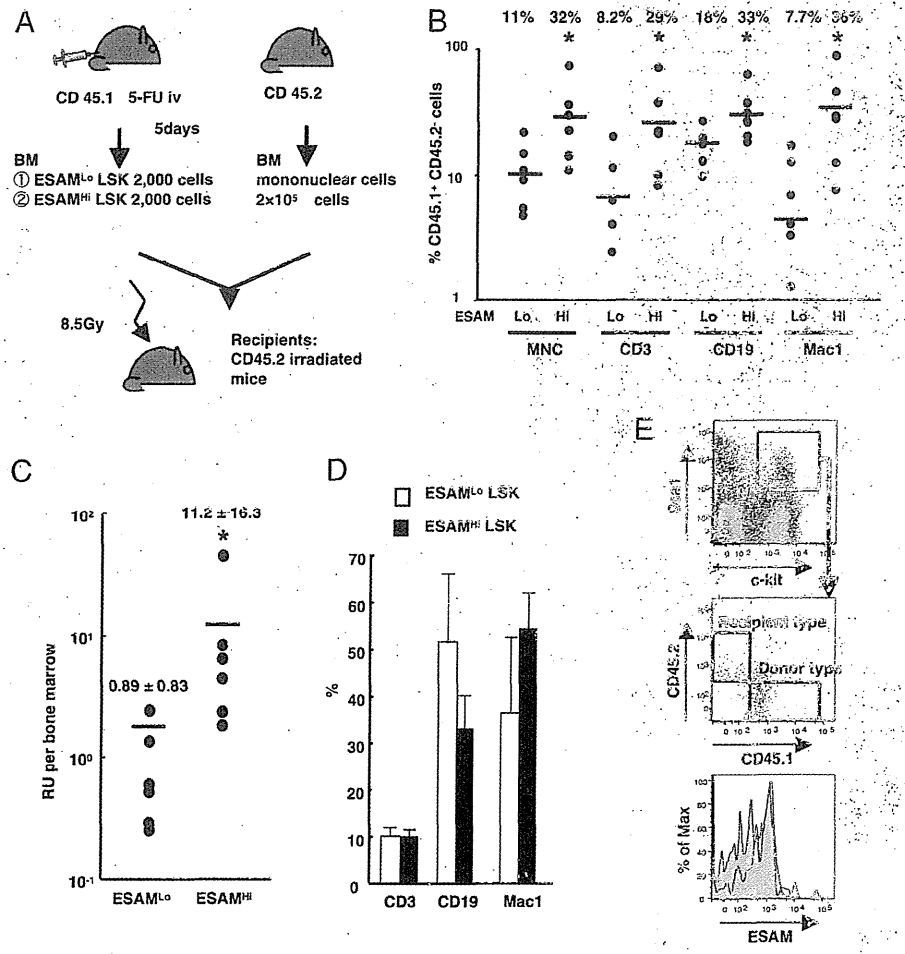

FIGURE 5. High ESAM expression correlates with long-term reconstituting HSC in 5-FU–treated mice BM. CD45.1 mice treated with single i.v. 150 mg/kg 5-FU were killed 5 d after treatment, and ESAM^{lo} or ESAM^{hi} LSK cells were sorted. Then, 2000 cells of each fraction were mixed with 2×10^5 CD45.2$^+$ whole adult BM cells and were transplanted to lethally irradiated CD45.2 WT mice ($n = 6$/group). (**A**) Scheme of the transplantation protocol. (**B**) Sixteen weeks after transplantation, all recipients were killed, and the contribution of transplanted CD45.1$^+$ ESAM^{lo} or ESAM^{hi} LSK cells was evaluated in BM. Percentages of the CD45.1$^+$CD45.2$^-$ population among CD45$^+$ mononuclear cells (MNC), CD3e$^+$, CD19$^+$, or Mac1$^+$ cells of each recipient were plotted. Numbers above the dots indicate mean percentages. (**C**) RU per BM of each recipient are plotted. Numbers above the dots indicate mean RU per BM ± SD. (B and C) The statistically significant differences between ESAM^{lo} and ESAM^{hi} LSK transplanted mice are shown. (**D**) The percentages of CD3e$^+$, CD19$^+$, or Mac1$^+$ cells among the CD45.1$^+$ cells of recipient BM are shown. The data from the ESAM^{lo} (open bars) and ESAM^{hi} (filled bars) LSK recipients are shown. The results are shown as means ± SD. (**E**) Flow cytometry profiles of the LSK fraction were examined in the ESAM^{hi} LSK recipients 16 wk after transplantation. The *top panel* shows the c-Kit and Scal expression on the Lin$^-$ fraction. The *middle panel* shows the CD45.1 and CD45.2 profile on the LSK fraction. Two frames in the *middle panel* indicate CD45.1$^+$CD45.2$^-$ LSK (donor-type) or CD45.1$^-$CD45.2$^+$ LSK (competitor-type) fraction, respectively. In the *bottom panel*, the tinted line shows the ESAM level of donor-type LSK, and the solid line shows that of competitors. The data shown represent one of two independent transplant experiments that gave similar results. *$p < 0.05$.

μm from vascular endothelium. Because the distance of 20 μm is approximate to three hematopoietic cell diameters, most activated HSC at day 5 of 5-FU treatment were probably adjacent or close to the vascular endothelium. These observations suggested that activated ESAM^{hi} HSC can be intimate with endothelial cells and/or vascular-related cells.

Hematopoietic recovery after BM stress is compromised in ESAM-deficient mice

The results above suggested that ESAM expression levels mirror HSC shifts between quiescence and activation after BM injury. However, it remained unclear whether ESAM plays any role in physiological hematopoietic recovery. To address this issue, we evaluated hematopoietic recovery of ESAM KO mice after 5-FU injection. We did not observe significant phenotypes in peripheral blood of homeostatic ESAM KO mice except for slight anemia. Intriguingly, after injecting 200 mg/kg 5-FU, the KO mice had more severe pancytopenia than did WT mice (Fig. 7A). Whereas leukocyte and platelet counts recovered by day 10, severe anemia was protracted in KO mice (hemoglobin, WT 10.4 ± 1.1 g/dl versus KO 6.0 ± 1.7 g/dl at day 10), and three of nine KO mice died before full hematopoietic recovery (Fig. 7B). With respect to the BM, ESAM deficiency did not affect numbers of total mononuclear, LSK, or Flt3$^-$ LSK cells at days 0 and 5 after 5-FU. However, all categories were significantly reduced compared with WT mice at day 8 after 5-FU (Fig. 7C). Considering that hematopoietic recovery happened after day 5, when ESAM upregulation on HSC peaked, these results suggested that ESAM is indispensable for normal hematopoietic recovery after BM injury.

NF-κB and topoisomerase II are likely important for ESAM upregulation in HSC

Next, we searched the promoter sequence of the ESAM gene to find molecular mechanisms possibly involved in ESAM upregulation

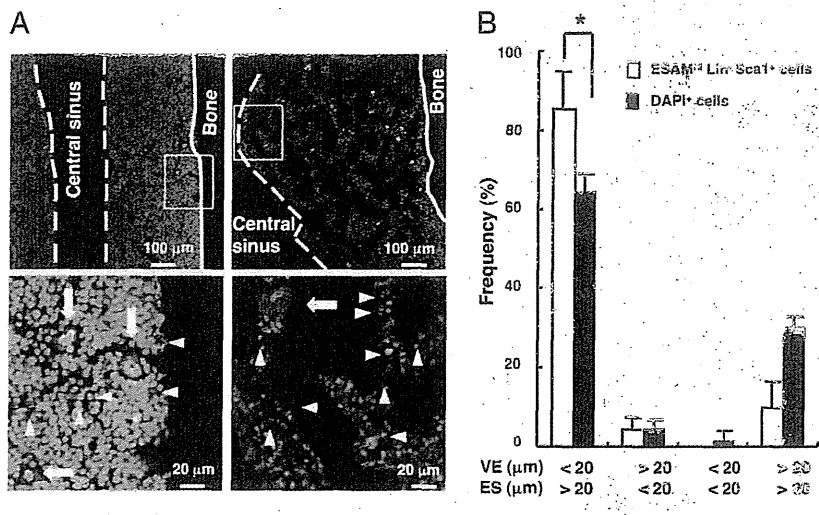

FIGURE 6. ESAM^{hi} HSC at day 5 after 5-FU injection are mainly localized around vascular areas. (**A**) BM sections from C57BL/6 mice were stained with Abs against ESAM (red), Sca1 (blue), and Lin (Gr1, B220, CD3e, CD8, and Ter119) sets (green). The nuclei of the cells are labeled with DAPI. The *left panels* are representative images of a BM section of untreated mouse, and the *right panels* are from the mouse 5 d after a 5-FU treatment (150 mg/kg). The frames in the *upper panels* are zoomed in to the *lower panels*. In the *lower panels*, ESAM^{hi} large cells are megakaryocytes (arrows). ESAM$^+$Lin$^-$Sca1$^+$ cells are indicated by arrowheads. (**B**) The distances from each ESAM$^+$Lin$^-$Sca1$^+$ cell to the vascular endothelium (VE) and to the endosteum (ES) were measured, and their distribution frequencies were evaluated for 5-FU–treated BM. Open bars show the frequencies for 50 ESAM^{hi}Lin$^-$Sca1$^+$ cells each in four separate specimens. As controls, random 100 DAPI$^+$ cells each in the same specimens were evaluated (filled bars). The cells were classified into four categories: close to VE (within 20 μm) but not close to ES (>20 μm); close to ES but not close to VE; close to both ES and VE; not close to either ES or VE. $*p < 0.05$.

(Fig. 8A). An NF-κB binding sequence at 363 bp upstream of the ESAM exon 1 drew our attention because it was well known to be an antiapoptotic factor after cell injury (27). We also found upregulation of NF-κB in the BM LSK cells after 5-FU treatment (data not shown). To examine the possible involvement of NF-κB, we administered bortezomib, a proteasome-inhibiting drug whose main action is inhibition of NF-κB, to 5-FU–treated mice (Fig. 8B). We found that bortezomib partially cancelled the ESAM upregulation caused by 5-FU injection (mean fluorescence intensity, 4790 ± 497 with 5-FU alone, 4090 ± 1050 with 5-FU and bortezomib) (Fig. 8C). Then, we conducted luciferase reporter assays to confirm the importance of the NF-κB binding sequence for ESAM transcription (Fig. 8E). We used endothelial bEnd3 cells that constantly express high levels of ESAM. The luciferase activity remarkably decreased from construct A to B (Fig. 8F).

Although the above data suggested that NF-κB was likely involved in ESAM upregulation of HSC, they also implied that other molecules should be involved. The luciferase reporter activity

A

WT	Day 0	Day 5	Day 10
WBC (/μl)	3060±684	4680±622	5160±493
RBC (×10^4 /μl)	962±78	877±29	716±73
Hb (g/dl)	14.8±1.3	13.2±0.5	10.4±1.1
Plt (×10^4 /μl)	87.7±8.3	52.3±6.0	171.1±36.0

ESAM KO	Day 0	Day 5	Day 10
WBC (/μl)	3540±1607	3000±212 **	4425±2642
RBC (×10^4 /μl)	859±35 *	794±48 *	418±114 **
Hb (g/dl)	12.8±0.5 *	11.6±0.8 **	6.0±1.7 **
Plt (×10^4 /μl)	93.1±7.9	38.3±2.0 **	213.3±38.4

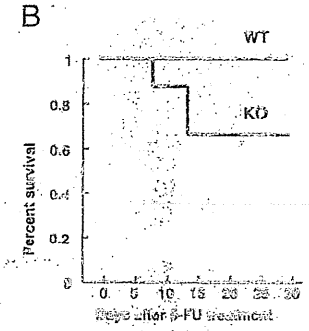

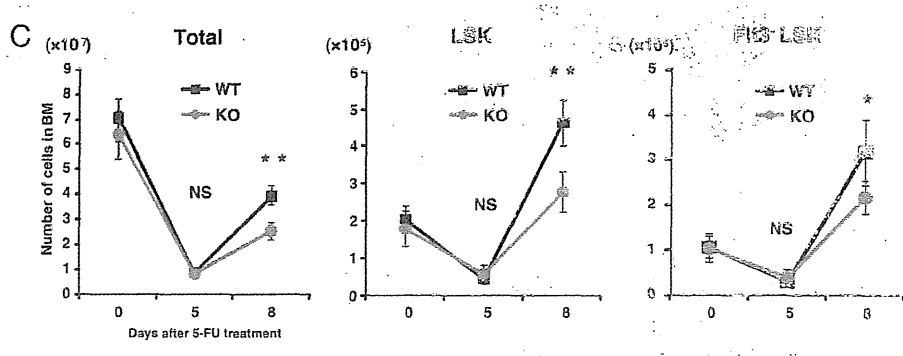

FIGURE 7. ESAM is required for normal hematopoietic recovery after BM injury. (**A**) Peripheral blood was examined every 5 d after single 200 mg/kg 5-FU treatment to WT or ESAM KO mice ($n = 5$ in each). All mice were 8-wk-old males. WBC, RBC, hemoglobin (Hb), and platelet (Plt) counts were compared between WT and ESAM KO mice at each time point. The results are shown as means ± SD. (**B**) Kaplan–Meier survival curves are shown regarding WT or ESAM KO mice treated with single 200 mg/kg 5-FU ($n = 9$ in each). (**C**) Total mononuclear cells (MNC), LSK cells, and Flt3$^-$ LSK cells in BM of WT or ESAM KO mice were evaluated at day 0 (homeostatic state), day 5, and day 8 after 150 mg/kg 5-FU treatment. The results are shown as means ± SD of five mice. $*p < 0.05$, $**p < 0.01$.

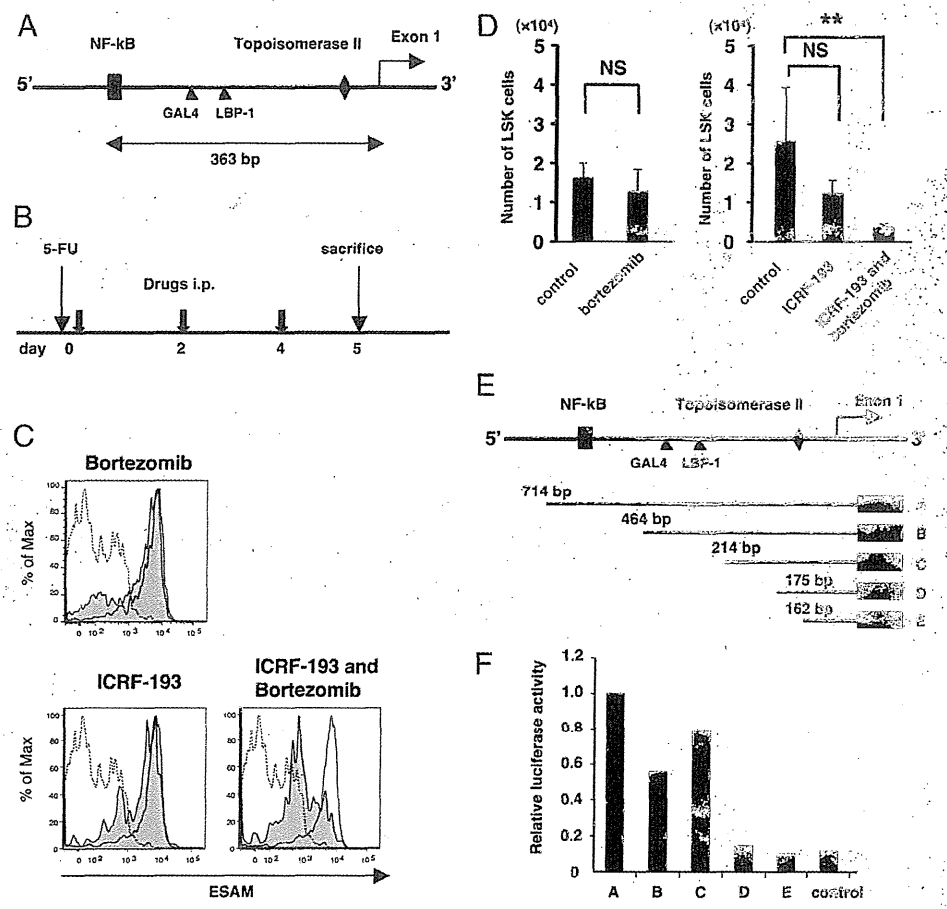

FIGURE 8. NF-κB and topoisomerase II regulate ESAM transcription. (**A**) Schematic figure regarding the upstream region of genomic ESAM DNA. Each transcription molecule is thought to work at indicated point. The distances between the beginning of topoisomerase II or NF-κB working site and the beginning of ESAM exon 1 are shown. (**B–D**) C57BL/6 mice treated with 5-FU (150 mg/kg) on day 0 were i.p. administered 1 mg/kg bortezomib and/or 6 mg/kg ICRF-193 on days 0, 2, and 4 after a 5-FU injection. Control mice were treated with solvents (saline or DMSO), in addition to 5-FU. (C) Flow cytometry analyses were performed with respect to the ESAM expression on BM LSK fraction on day 5. The dashed lines show ESAM levels of 5-FU of day 0, the open histograms with solid lines show the control ESAM levels of day 5, and the tinted lines show those of mice treated with indicated drugs after a 5-FU injection. Representative results are shown. Each group had at least three mice and showed similar results. (D) The numbers of LSK cells from a pair of femora and tibiae at day 5 of each group were evaluated. Each group had at least three mice. The results are shown as means ± SD. (**E**) Schematic figure of the luciferase assay constructs. There were topoisomerase II and NF-κB working sites upstream of exon 1 of the ESAM gene in the DNA sequence. Construct A contains both working sites. Constructs B–D contain the topoisomerase II working site. Construct E does not contain any working sites. Each DNA segment was amplified by PCR and inserted in the pGL3 basic vector. Each number (bp) is the distance from the 5′ end of each construct to the exon 1. (**F**) Luciferase assays were performed using the endothelial bEnd3 cell line. Each pGL3-promoter construct and pRL-CMV encoding the *Renilla* luciferase gene were transfected into the cells by Lipofectamine. Empty vector was used as control. Relative luciferase activity is adjusted such that construct A is 1.0. The data are shown as one of three independent experiments that gave similar results. $^{**}p < 0.01$.

sharply decreased from construct C to D probably because DNA sequences between the two are necessary for binding of the basic transcription complex. Immediately downstream of that site, we found a consensus sequence for cleavage by topoisomerase II (28). Because topoisomerase II was also known to correlate with HSC activation, we tested ICRF-193, a topoisomerase II-specific inhibitor, in 5-FU–treated mice. Similar to bortezomib, ICRF-193 partially inhibited the ESAM upregulation (mean fluorescence intensity, 3260 ± 685 with 5-FU and ICRF-193) (Fig. 8C). Interestingly, the ESAM upregulation was remarkably abrogated when bortezomib and ICRF-193 were administered simultaneously (mean fluorescence intensity, 1980 ± 392 with 5-FU, bortezomib, and ICRF-193) (Fig. 8C). The mice treated with bortezomib and ICRF-193 showed significant reduction of LSK cells compared with control mice at day 5, although the mice treated with a single inhibitory drug did not respond in that way (Fig. 8D). These results indicated that NF-κB and topoisomerase II synergistically regulate ESAM expression on HSC after BM injury.

Discussion

Although adult stem cells divide infrequently, they have high proliferative capacity. Emerging evidence suggests that both quiescent and active stem cells simultaneously exist in different but consecutive niches under normal steady-state conditions (9). It is also well known that the quiescent stem cells proliferate after wounding or transplantation (5, 29). Accurate identification of stem cells according to their proliferative states is essential to understand the biological nature of "stemness" and to develop tissue-regeneration therapies. We now report that ESAM, a new marker for HSC, represents a powerful tool to monitor the transition of HSC between quiescence and activation after BM injury. Furthermore, ESAM is required for normal recovery from marrow ablation.

Treatment of mice with 5-FU enriches primitive HSC by eliminating most proliferating progenitors while sparing non-cycling quiescent HSC. Additionally, 5-FU has been widely used to stimulate quiescent adult HSC to proliferate (8, 30–33). In the present study, we exploited this method to evaluate whether ESAM levels would change, and we observed dramatic upregulation. Previous studies showed that expression levels of many adult HSC markers change during hematopoietic recovery after 5-FU–mediated myeloablation. Whereas expression of c-Kit and N-cadherin decrease, levels of Mac1, CD34, and AA4 that are markers for fetal HSC revive (8, 31, 33). CD150 and Sca1 are also known to increase on activated HSC, as confirmed in our study (see Fig. 2A, Supplemental Fig. 1). However, we stress that the degree of change in ESAM greatly exceeds that of other markers. The ESAM^{hi} LSK fraction includes more LT-HSC defined by SLAM markers than does the ESAM^{lo} subset (Fig. 2A, *right panels*). However, it is controversial whether HSC can only be found in the CD150^{+} fraction (34, 35). For that reason, we did not use SLAM family markers to purify HSC when analyzing functions of ESAM.

Our cell cycle analyses showed that virtually all ESAM^{hi}Sca1^{+}c-Kit^{+} cells after 5-FU treatment exit the G_0 phase (Fig. 3). Alternatively, long-term repopulating HSC can be enriched in the ESAM^{hi} fraction (Fig. 5B, 5C). These results suggest that the ESAM^{hi} LSK fraction includes cycling, long-term multipotent HSC. Our data are in accordance with a previous report by Haug et al. (31) showing that the N-cadherin^{lo} HSC in 5-FU–treated BM have high cell cycle entry rates and, at the same time, robust long-term reconstituting potential. These features do not match those of adult HSC under steady-state, but rather are reminiscent of fetal HSC. It is interesting that activated adult HSC after BM injury resemble fetal HSC regarding not only cell cycle status but also surface markers.

Although it was reported that the LSK Thy1^{lo} Flk2/Flt3^{-} fraction in mobilized BM contains authentic HSC less frequently than those in untreated BM (36), our present data have demonstrated that HSC of 5-FU–treated BM can effectively reconstitute long-term hematopoiesis. One interpretation for the discrepancy is that because the HSC change their phenotype by activation, our sorting method, which depended on high expression of ESAM, might have enriched the authentic HSC more efficiently than did the conventional sorting gate. Another possibility is that active cycling and good engraftment may not be mutually exclusive. Indeed, some previous reports showed that cycling HSC are not necessarily incapable of engraftment when transplanted (37, 38). Transplanted ESAM^{hi} LSK cells reconstituted the ESAM^{lo} LSK fraction in lethally irradiated recipients 16 wk after transplantation, suggesting that the ESAM^{hi} subset could keep its stemness even after entering cell cycle. Of note, ESAM levels return to homeostatic levels by 12 d after 5-FU injection.

Previous studies used high-resolution real-time imaging systems to show that transplanted HSC tend to first home to the endosteum in irradiated mice (39, 40). Our immunohistochemical analyses showed that most ESAM^{hi} HSC in BM at day 5 following 5-FU treatment were localized within 20 μm from vascular endothelium. As previously predicted by Venezia et al. (33), quiescent HSC might need to once pause in the endosteum so that they can prepare to proliferate. After receiving unknown signals, they migrate to a proliferative zone, which is presumably composed of vascular endothelial cells. ESAM might help HSC to receive the proliferative signals from ESAM^{+} endothelial cells because ESAM mediates cell–cell adhesion through homophilic interactions (11). Alternatively, the endosteum and the sinusoidal vascular area might cooperatively form a proliferative environment for HSC. We observed that sinusoidal vasculature spaces and perivascular areas are remarkably enlarged in BM after 5-FU treatment (Fig. 6A). Indeed, a previous study showed that many osteoblasts are adjacent to or in proximity to vasculature in 5-FU–treated BM (39). Therefore, the ESAM^{hi} HSC interacting with endothelial cells simultaneously may receive signals from endosteal niches. Recently, it has been reported that the nervous system and glial cells play important roles in the HSC niche (41, 42). It would be important to examine how the ESAM^{hi} HSC interact with CXCL12-abundant reticular cells or glial cells because they are key components of both HSC niches (21).

Additional endothelial or other Ags whose expression levels are enhanced by BM injury might be functionally involved in activated HSC. However, no apparent phenotypes with either CD34 or CD150 KO mice have been documented (1, 43). In contrast, our new findings strongly suggest that ESAM is indispensable for normal hematopoietic recovery after BM injury. ESAM KO mice do not show hematopoietic defects except for slight anemia (Fig. 7) (44). However, hematopoietic recovery after BM injury was significantly compromised in the ESAM KO mice, suggesting its importance under stress conditions. Especially, the deficiency caused significant anemia after 5-FU treatment, and some KO mice with severe anemia died before BM recovery. Thus, ESAM might be particularly important for demand erythropoiesis. Because ESAM^{hi} HSC closely interact with ESAM^{+} vascular endothelial cells (Fig. 6), HSC might receive necessary signals directly or indirectly via interaction with ESAM. In fact, ESAM deficiency resulted in insufficient Rho signaling in endothelial cells, which potentially regulates the stabilization of endothelial tight junctions (13). Rho is also expressed in hematopoietic progenitors and involved in their polarity and mobility (45). Further studies are necessary to learn precisely how ESAM controls HSC function during BM recovery.

It is very important to know how ESAM expression is regulated in HSC. NF-κB is known to be activated by BM stress and induces cyclin D1, a key regulator of the G_1 check point (46). Indeed, we observed upregulation of NF-κB in HSC after 5-FU treatment (data not shown). Topoisomerase II is required for the G_0-to-S phase transition in mammalian cells (47). NF-κB was implicated as a key ESAM transcription factor by luciferase assay (Fig. 8F). In addition to NF-κB, we focused on topoisomerase II, because this enzyme is required for regulated transcription (48). Although independent administration of inhibitors for each factor showed only subtle effects on ESAM levels, the drugs synergistically but still partially abrogated the ESAM upregulation in 5-FU–treated HSC (Fig. 8C). Decreased ESAM expression with combined bortezomib and ICRF-193 treatment had a suppressive effect on the number of LSK cells, although treatment of a single inhibitory drug did not have significant effects (Fig. 8D). Given that ESAM KO mice did not show significant cytopenia at 5-FU day 5 compared with WT mice (Fig. 7C), bortezomib and ICRF-193 may suppress cell cycle-related pathways other than ESAM. Recently, reactive oxygen species (ROS) are attracting attention because levels in HSC influence their cell cycle status, self-renewal ability, and differentiation potential (49, 50). Accumulation of ROS is known to activate NF-κB signaling (51). Additionally, several studies have suggested that accumulation of ROS is likely involved in HSC aging (52–54). We reported that whereas ESAM levels on the LSK fraction decrease after the neonatal period, they increase again with aging (16). Bowie et al. (7) previously proved that fetal type HSC change their self-renewal and differentiation properties to be quiescent at 4 wk after birth when blood cell outputs reach homeostasis. Alternatively, several reports showed that absolute numbers of phenotypic HSC increase by 3- to 10-

fold in aged mouse BM (55–57). At present, we are studying whether intracellular ROS levels and related signaling pathways might be involved in ESAM fluctuation on HSC, not only after BM stress but also in the context of aging.

In summary, our data have shown that ESAM can be valuable for purifying proliferating HSC. Information from those HSC will give us important insights regarding essential molecules for HSC expansion. Additionally, the data from ESAM KO mice have suggested that high ESAM expression on HSC is likely to play important roles for hematopoietic recovery after BM injury. Further studies should address physiological meanings of the fluctuation of ESAM levels according to the HSC status.

Acknowledgments

We thank Drs. Stefan Butz and Dietmar Vestweber (Max Planck Institute) for a rat anti-mouse ESAM Ab and Drs. Michiko Ichii and Paul W. Kincade for many thoughtful suggestions on the manuscript.

Disclosures

The authors have no financial conflicts of interest.

References

1. Kiel, M. J., O. H. Yilmaz, T. Iwashita, O. H. Yilmaz, C. Terhorst, and S. J. Morrison. 2005. SLAM family receptors distinguish hematopoietic stem and progenitor cells and reveal endothelial niches for stem cells. *Cell* 121: 1109–1121.
2. Osawa, M., K. Hanada, H. Hamada, and H. Nakauchi. 1996. Long-term lymphohematopoietic reconstitution by a single CD34-low/negative hematopoietic stem cell. *Science* 273: 242–245.
3. Spangrude, G. J., S. Heimfeld, and I. L. Weissman. 1988. Purification and characterization of mouse hematopoietic stem cells. *Science* 241: 58–62.
4. Foudi, A., K. Hochedlinger, D. Van Buren, J. W. Schindler, R. Jaenisch, V. Carey, and H. Hock. 2009. Analysis of histone 2B-GFP retention reveals slowly cycling hematopoietic stem cells. *Nat. Biotechnol.* 27: 84–90.
5. Wilson, A., E. Laurenti, G. Oser, R. C. van der Wath, W. Blanco-Bose, M. Jaworski, S. Offner, C. F. Dunant, L. Eshkind, E. Bockamp, et al. 2008. Hematopoietic stem cells reversibly switch from dormancy to self-renewal during homeostasis and repair. *Cell* 135: 1118–1129.
6. Ema, H., and H. Nakauchi. 2000. Expansion of hematopoietic stem cells in the developing liver of a mouse embryo. *Blood* 95: 2284–2288.
7. Bowie, M. B., D. G. Kent, B. Dykstra, K. D. McKnight, L. McCaffrey, P. A. Hoodless, and C. J. Eaves. 2007. Identification of a new intrinsically timed developmental checkpoint that reprograms key hematopoietic stem cell properties. *Proc. Natl. Acad. Sci. USA* 104: 5878–5882.
8. Randall, T. D., and I. L. Weissman. 1997. Phenotypic and functional changes induced at the clonal level in hematopoietic stem cells after 5-fluorouracil treatment. *Blood* 89: 3596–3606.
9. Li, L., and H. Clevers. 2010. Coexistence of quiescent and active adult stem cells in mammals. *Science* 327: 542–545.
10. Wilson, A., and A. Trumpp. 2006. Bone-marrow haematopoietic-stem-cell niches. *Nat. Rev. Immunol.* 6: 93–106.
11. Hirata Ki, T., K. Ishida, M. Penta, E. Rezaee, J. Yang, Wohlgemuth, and T. Quertermous. 2001. Cloning of an immunoglobulin family adhesion molecule selectively expressed by endothelial cells. *J. Biol. Chem.* 276: 16223–16231.
12. Nasdala, I., K. Wolburg-Buchholz, H. Wolburg, A. Kuhn, K. Ebnet, G. Brachtendorf, U. Samulowitz, B. Kuster, B. Engelhardt, D. Vestweber, and S. Butz. 2002. A transmembrane tight junction protein selectively expressed on endothelial cells and platelets. *J. Biol. Chem.* 277: 16294–16303.
13. Wegmann, F., B. Petri, A. G. Khandoga, C. Moser, A. Khandoga, S. Volkery, H. Li, I. Nasdala, O. Brandau, R. Fässler, et al. 2006. ESAM supports neutrophil extravasation, activation of Rho, and VEGF-induced vascular permeability. *J. Exp. Med.* 203: 1671–1677.
14. Hara, T., T. Ishida, H. M. Cangara, and K. Hirata. 2009. Endothelial cell-selective adhesion molecule regulates albuminuria in diabetic nephropathy. *Microvasc. Res.* 77: 348–355.
15. Stalker, T. J., J. Wu, A. Morgans, E. A. Traxler, L. Wang, M. S. Chatterjee, D. Lee, T. Quertermous, R. A. Hall, D. A. Hammer, et al. 2009. Endothelial cell specific adhesion molecule (ESAM) localizes to platelet-platelet contacts and regulates thrombus formation in vivo. *J. Thromb. Haemost.* 7: 1886–1896.
16. Yokota, T., K. Oritani, S. Butz, K. Kokame, P. W. Kincade, T. Miyata, D. Vestweber, and Y. Kanakura. 2009. The endothelial antigen ESAM marks primitive hematopoietic progenitors throughout life in mice. *Blood* 113: 2914–2923.
17. Ogawa, M. 2002. Changing phenotypes of hematopoietic stem cells. *Exp. Hematol.* 30: 3–6.
18. Ishida, T., R. K. Kundu, E. Yang, K. Hirata, Y. D. Ho, and T. Quertermous. 2003. Targeted disruption of endothelial cell-selective adhesion molecule inhibits angiogenic processes in vitro and in vivo. *J. Biol. Chem.* 278: 34598–34604.
19. Inoue, M., T. Ishida, T. Yasuda, R. Toh, T. Hara, H. M. Cangara, Y. Rikitake, K. Taira, L. Sun, R. K. Kundu, et al. 2010. Endothelial cell-selective adhesion molecule modulates atherosclerosis through plaque angiogenesis and monocyte-endothelial interaction. *Microvasc. Res.* 80: 179–187.
20. Harrison, D. E., C. T. Jordan, R. K. Zhong, and C. M. Astle. 1993. Primitive hemopoietic stem cells: direct assay of most productive populations by competitive repopulation with simple binomial, correlation and covariance calculations. *Exp. Hematol.* 21: 206–219.
21. Sugiyama, T., H. Kohara, M. Noda, and T. Nagasawa. 2006. Maintenance of the hematopoietic stem cell pool by CXCL12-CXCR4 chemokine signaling in bone marrow stromal cell niches. *Immunity* 25: 977–988.
22. Yilmaz, O. H., M. J. Kiel, and S. J. Morrison. 2006. SLAM family markers are conserved among hematopoietic stem cells from old and reconstituted mice and markedly increase their purity. *Blood* 107: 924–930.
23. Arai, F., and T. Suda. 2007. Maintenance of quiescent hematopoietic stem cells in the osteoblastic niche. *Ann. N. Y. Acad. Sci.* 1106: 41–53.
24. Lerner, C., and D. E. Harrison. 1990. 5-Fluorouracil spares hemopoietic stem cells responsible for long-term repopulation. *Exp. Hematol.* 18: 114–118.
25. Yin, T., and L. Li. 2006. The stem cell niches in bone. *J. Clin. Invest.* 116: 1195–1201.
26. Morita, Y., H. Ema, and H. Nakauchi. 2010. Heterogeneity and hierarchy within the most primitive hematopoietic stem cell compartment. *J. Exp. Med.* 207: 1173–1182.
27. Wang, C. Y., J. C. Cusack, Jr., R. Liu, and A. S. Baldwin, Jr. 1999. Control of inducible chemoresistance: enhanced anti-tumor therapy through increased apoptosis by inhibition of NF-κB. *Nat. Med.* 5: 412–417.
28. Spitzner, J. R., and M. T. Muller. 1988. A consensus sequence for cleavage by vertebrate DNA topoisomerase II. *Nucleic Acids Res.* 16: 5533–5556.
29. Tumbar, T., G. Guasch, V. Greco, C. Blanpain, W. E. Lowry, M. Rendl, and E. Fuchs. 2004. Defining the epithelial stem cell niche in skin. *Science* 303: 359–363.
30. Harrison, D. E., and C. P. Lerner. 1991. Most primitive hematopoietic stem cells are stimulated to cycle rapidly after treatment with 5-fluorouracil. *Blood* 78: 1237–1240.
31. Haug, J. S., X. C. He, J. C. Grindley, J. P. Wunderlich, K. Gaudenz, J. T. Ross, A. Paulson, K. P. Wagner, Y. Xie, R. Zhu, et al. 2008. N-cadherin expression level distinguishes reserved versus primed states of hematopoietic stem cells. *Cell Stem Cell* 2: 367–379.
32. Sirin, O., G. L. Lukov, R. Mao, O. M. Conneely, and M. A. Goodell. 2010. The orphan nuclear receptor Nurr1 restricts the proliferation of haematopoietic stem cells. *Nat. Cell Biol.* 12: 1213–1219.
33. Venezia, T. A., A. A. Merchant, C. A. Ramos, N. L. Whitehouse, A. S. Young, C. A. Shaw, and M. A. Goodell. 2004. Molecular signatures of proliferation and quiescence in hematopoietic stem cells. *PLoS Biol.* 2: e301.
34. Kiel, M. J., O. H. Yilmaz, and S. J. Morrison. 2008. CD150$^-$ cells are transiently reconstituting multipotent progenitors with little or no stem cell activity. *Blood* 111: 4413–4414, author reply 4414–4415.
35. Weksberg, D. C., S. M. Chambers, N. C. Boles, and M. A. Goodell. 2008. CD150$^-$ side population cells represent a functionally distinct population of long-term hematopoietic stem cells. *Blood* 111: 2444–2451.
36. Passegué, E., A. J. Wagers, S. Giuriato, W. C. Anderson, and I. L. Weissman. 2005. Global analysis of proliferation and cell cycle gene expression in the regulation of hematopoietic stem and progenitor cell fates. *J. Exp. Med.* 202: 1599–1611.
37. Steinman, R. A. 2002. Cell cycle regulators and hematopoiesis. *Oncogene* 21: 3403–3413.
38. Wilpshaar, J., J. H. Falkenburg, X. Tong, W. A. Noort, R. Breese, D. Heilman, H. Kanhai, C. M. Orschell-Traycoff, and E. F. Srour. 2000. Similar repopulating capacity of mitotically active and resting umbilical cord blood CD34$^+$ cells in NOD/SCID mice. *Blood* 96: 2100–2107.
39. Lo Celso, C., H. E. Fleming, J. W. Wu, C. X. Zhao, S. Miake-Lye, J. Fujisaki, D. Côté, D. W. Rowe, C. P. Lin, and D. T. Scadden. 2009. Live-animal tracking of individual haematopoietic stem/progenitor cells in their niche. *Nature* 457: 92–96.
40. Xie, Y., T. Yin, W. Wiegraebe, X. C. He, D. Miller, D. Stark, K. Perko, R. Alexander, J. Schwartz, J. C. Grindley, et al. 2009. Detection of functional haematopoietic stem cell niche using real-time imaging. *Nature* 457: 97–101.
41. Katayama, Y., M. Battista, W. M. Kao, A. Hidalgo, A. J. Peired, S. A. Thomas, and P. S. Frenette. 2006. Signals from the sympathetic nervous system regulate hematopoietic stem cell egress from bone marrow. *Cell* 124: 407–421.
42. Yamazaki, S., H. Ema, G. Karlsson, T. Yamaguchi, H. Miyoshi, S. Shioda, M. M. Taketo, S. Karlsson, A. Iwama, and H. Nakauchi. 2011. Nonmyelinating Schwann cells maintain hematopoietic stem cell hibernation in the bone marrow niche. *Cell* 147: 1146–1158.
43. Cheng, J., S. Baumhueter, G. Cacalano, K. Carver-Moore, H. Thibodeaux, R. Thomas, H. E. Broxmeyer, S. Cooper, N. Hague, M. Moore, and L. A. Lasky. 1996. Hematopoietic defects in mice lacking the sialomucin CD34. *Blood* 87: 479–490.
44. Ooi, A. G., H. Karsunky, R. Majeti, S. Butz, D. Vestweber, T. Ishida, T. Quertermous, I. L. Weissman, and E. C. Forsberg. 2009. The adhesion molecule Esam1 is a novel hematopoietic stem cell marker. *Stem Cells* 27: 653–661.
45. Fonseca, A. V., D. Freund, M. Bornhäuser, and D. Corbeil. 2010. Polarization and migration of hematopoietic stem and progenitor cells rely on the RhoA/ROCK I pathway and an active reorganization of the microtubule network. *J. Biol. Chem.* 285: 31661–31671.
46. Hinz, M., D. Krappmann, A. Eichten, A. Heder, C. Scheidereit, and M. Strauss. 1999. NF-κB function in growth control: regulation of cyclin D1 expression and G_0/G_1-to-S-phase transition. *Mol. Cell. Biol.* 19: 2690–2698.

47. Hossain, M. S., N. Akimitsu, T. Takaki, H. Hirai, and K. Sekimizu. 2002. ICRF-193, a catalytic inhibitor of DNA topoisomerase II, inhibits re-entry into the cell division cycle from quiescent state in mammalian cells. *Genes Cells* 7: 285–294.
48. Ju, B. G., V. V. Lunyak, V. Perissi, I. Garcia-Bassets, D. W. Rose, C. K. Glass, and M. G. Rosenfeld. 2006. A topoisomerase IIβ-mediated dsDNA break required for regulated transcription. *Science* 312: 1798–1802.
49. Jang, Y. Y., and S. J. Sharkis. 2007. A low level of reactive oxygen species selects for primitive hematopoietic stem cells that may reside in the low-oxygenic niche. *Blood* 110: 3056–3063.
50. Orford, K. W., and D. T. Scadden. 2008. Deconstructing stem cell self-renewal: genetic insights into cell-cycle regulation. *Nat. Rev. Genet.* 9: 115–128.
51. Morgan, M. J., and Z. G. Liu. 2011. Crosstalk of reactive oxygen species and NF-κB signaling. *Cell Res.* 21: 103–115.
52. Ito, K., A. Hirao, F. Arai, S. Matsuoka, K. Takubo, I. Hamaguchi, K. Nomiyama, K. Hosokawa, K. Sakurada, N. Nakagata, et al. 2004. Regulation of oxidative stress by ATM is required for self-renewal of haematopoietic stem cells. *Nature* 431: 997–1002.
53. Liu, J., L. Cao, J. Chen, S. Song, I. H. Lee, C. Quijano, H. Liu, K. Keyvanfar, H. Chen, L. Y. Cao, et al. 2009. Bmi1 regulates mitochondrial function and the DNA damage response pathway. *Nature* 459: 387–392.
54. Tothova, Z., R. Kollipara, B. J. Huntly, B. H. Lee, D. H. Castrillon, D. E. Cullen, E. P. McDowell, S. Lazo-Kallanian, I. R. Williams, C. Sears, et al. 2007. FoxOs are critical mediators of hematopoietic stem cell resistance to physiologic oxidative stress. *Cell* 128: 325–339.
55. Kim, M., H. B. Moon, and G. J. Spangrude. 2003. Major age-related changes of mouse hematopoietic stem/progenitor cells. *Ann. N. Y. Acad. Sci.* 996: 195–208.
56. Morrison, S. J., A. M. Wandycz, K. Akashi, A. Globerson, and I. L. Weissman. 1996. The aging of hematopoietic stem cells. *Nat. Med.* 2: 1011–1016.
57. Sudo, K., H. Ema, Y. Morita, and H. Nakauchi. 2000. Age-associated characteristics of murine hematopoietic stem cells. *J. Exp. Med.* 192: 1273–1280.

ELSEVIER

Experimental Hematology

Experimental Hematology 2012;40:724–737

CML cells expressing the TEL/MDS1/EVI1 fusion are resistant to imatinib-induced apoptosis through inhibition of BAD, but are resensitized with ABT-737

Kazuyuki Shimada[a,b,c], Akihiro Tomita[b], Yosuke Minami[b], Akihiro Abe[b,d], Charlotte K. Hind[c], Hitoshi Kiyoi[b], Mark S. Cragg[c], and Tomoki Naoe[b]

[a]*Institute for Advanced Research, Nagoya University, Nagoya, Japan;* [b]*Department of Hematology and Oncology, Nagoya University Graduate School of Medicine, Nagoya, Japan;* [c]*Antibody and Vaccine Group, Cancer Sciences Unit, Faculty of Medicine, University of Southampton, Southampton General Hospital, Southampton, UK;* [d]*Department of Hematology, Fujita Health University School of Medicine, Toyoake, Aichi, Japan*

(Received 26 January 2012; revised 2 May 2012; accepted 19 May 2012)

Chronic myeloid leukemia is the first disease in which the potential of molecular targeted therapy with tyrosine kinase inhibitors (TKIs) was realized. Despite this success, a proportion of patients, particularly with advanced disease, are, or become, resistant to this treatment. Overcoming resistance and uncovering the underlying mechanisms is vital for further improvement of clinical outcomes. Here we report the identification, development, and characterization of a novel chronic myeloid leukemia cell line carrying the additional chromosomal aberration t(3;12)(q26;p13) resulting in expression of the TEL/MDS1/EVI1 fusion protein, which is resistant to TKIs. Resistance to TKIs was overcome by the co-administration of the BH3-mimetic, ABT-737. In addition, application of EVI1-specific small interfering RNA decreased expression of the TEL/MDS1/EVI1 fusion, reduced resistance to imatinib, and increased sensitivity to ABT-737. Subsequent studies revealed a role for the BH3-only protein BAD, probably via a phosphoinositide 3-kinase/AKT-dependent pathway, as pharmacological inhibition of AKT could also resensitize cells to death from TKIs. These findings indicate a novel pathway of TKI resistance regulated by EVI1 proteins and provide a promising means for overcoming resistance in chronic myeloid leukemia and other hematological malignancies displaying EVI1 overexpression.

Chronic myeloid leukemia (CML) is characterized by the presence of the *BCR-ABL* fusion gene. Its powerful transforming potential results in cells with a strong proliferation advantage, which are refractive to apoptosis and independent of extracellular survival signals [1–3]. However, development of BCR-ABL inhibitors, imatinib, dasatinib, and nilotinib has revealed the Achilles heel aspect of this potent oncogenic kinase and has heralded in an era of targeted therapy [4–6]. These drugs eliminate signaling downstream of BCR-ABL and result in profound growth arrest and apoptosis. The resulting clinical efficacy of TKI in CML has lead to them replacing interferon-α as first-line therapy. However, although clinical efficacy is generally excellent in early-stage CML, once the disease has progressed from benign chronic phase into an accelerated phase or blast crisis, i.e., advanced disease, the clinical outcome is generally poor [4,7,8]. Thus, preventing disease progression and stabilizing the disease in chronic phase have been the guiding principles of CML treatment to date.

The mechanism of TKI resistance observed in a proportion of patients can be either BCR-ABL–dependent or –independent [9]. BCR-ABL–dependent mechanisms are characterized by the emergence of mutations in the tyrosine kinase domain, including the T315I mutation, and/or overexpression of the BCR-ABL protein due to gene amplification [10]. BCR-ABL–independent mechanisms are characterized by dysregulations in drug transport [11,12], protection in

Drs. Cragg and Naoe contributed equally to this study and are the joint senior authors.

Offprint requests to: Kazuyuki Shimada, M.D., Ph.D., Institute for Advanced Research/Graduate School of Medicine, Department of Hematology and Oncology, Nagoya University Graduate School of Medicine, 65 Tsurumai-cho, Showa-ku, Nagoya 466-8550, Japan; E-mail: kshimada@med.nagoya-u.ac.jp

Supplementary data related to this article can be found online at http://dx.doi.org/10.1016/j.exphem.2012.05.007.

http://dx.doi.org/10.1016/j.exphem.2012.05.007